UNIVERSITY of CAMBRIDGE

DIRECT OBSERVATION OF FRACTURE OF CAS–GLASS/SiC COMPOSITES AND PROCESSING OF TOUGHENED ALUMINA

CUED/C–MATS/TR203
September, 1992

H.R. Shercliff[1], G. Vekinis[2],
M.F. Ashby[1] and P.W.R. Beaumont[1]

Department of Engineering

TECHNICAL REPORT

2

Air Force Office of Scientific Research
United States Air Force

Grant no. AFOSR–87–0307

Final Report to April, 1992

DIRECT OBSERVATION OF FRACTURE OF CAS–GLASS/SiC COMPOSITES AND PROCESSING OF TOUGHENED ALUMINA

CUED/C–MATS/TR203
September, 1992

H.R. Shercliff[1], G. Vekinis[2],
M.F. Ashby[1] and P.W.R. Beaumont[1]

[1] Engineering Department
Cambridge University
Trumpington St
Cambridge
CB2 1PZ, U.K.

[2] "Demokritos" National Centre for Scientific Research
Institute of Materials Science
15310 Ag. Paraskevi Attikis
P.O. Box 60228
Athens, Greece

REPORT DOCUMENTATION PAGE

Form Approved
OMB No. 0704-0188

1. AGENCY USE ONLY (Leave blank)	2. REPORT DATE	3. REPORT TYPE AND DATES COVERED
	September 1992	Final Report 1 April 1991 - 31 March 1992

4. TITLE AND SUBTITLE

Development and Characterization of Tough Ceramic Matrix Composites

5. FUNDING NUMBERS

AFOSR-91-0221

6. AUTHOR(S)

H.R. Shercliff, G. Vekinis,
M.F. Ashby, P.W.R. Beaumont

7. PERFORMING ORGANIZATION NAME(S) AND ADDRESS(ES)

Cambridge University
Engineering Department
Trumpington Street
Cambridge CB2 1PZ

8. PERFORMING ORGANIZATION REPORT NUMBER

CUED/C-MATS/TR203

AFOSR-TR- 93 0582

9. SPONSORING/MONITORING AGENCY NAME(S) AND ADDRESS(ES)

Sponsoring Agency: Air Force Office of Scientific Research
Bolling AFB, DC 20332-6448
Sponsoring/Monitoring Agency: European Office of Aerospace Research & Development, PSC 802 Box 14, FPO Ae 09499-0200

10. SPONSORING/MONITORING AGENCY REPORT NUMBER

11. SUPPLEMENTARY NOTES

12a. DISTRIBUTION/AVAILABILITY STATEMENT

Approved for Public Release
Distribution Unlimited

12b. DISTRIBUTION CODE

13. ABSTRACT (Maximum 200 words)

The first part of the report describes the continuation of a test series which has been undertaken on the laminated CAS-glass SiC fibre reinforced material provided by the USAF Materials Laboratory, Dayton, Ohio. Fracture mechanisms have been studied in four-point bend and in two geometries - double cantilever beam and double edge-notched tension. Dynamic in-situ scanning electron microscopy has enabled a clear charactisation of sub-critical damage, and crack interactions prior to final failure, both of which have a strong influence on the material failure strength.

The second part of the report describes preliminary studies on the fracture behaviour of alumina toughened with ductile metal reinforcements. Specimens of alumina reinforced with discrete particles (mainly cobalt) have been produced by pretreating metal powders and mixing them with alumina powder followed by sintering under protective atmospheres. Processing conditions have been developed, and fracture surfaces studied in the scanning electron microscope. Crack bridging by metal ligaments has been observed. The ligaments fail by necking and/or shearing. The materials and processing route appear to be promising, especially in terms of controlling the interfacial reactions and strength.

14. SUBJECT TERMS	15. NUMBER OF PAGES
Ceramic composites; crack growth mechanisms; scanning electron microscopy; models of fracture; toughness measurements; processing tough ceramic systems.	16. PRICE CODE

17. SECURITY CLASSIFICATION OF REPORT	18. SECURITY CLASSIFICATION OF THIS PAGE	19. SECURITY CLASSIFICATION OF ABSTRACT	20. LIMITATION OF ABSTRACT
UNCLASSIFIED	UNCLASSIFIED	UNCLASSIFIED	UNCLASSIFIED

GENERAL INSTRUCTIONS FOR COMPLETING SF 298

The Report Documentation Page (RDP) is used in announcing and cataloging reports. It is important that this information be consistent with the rest of the report, particularly the cover and title page. Instructions for filling in each block of the form follow. It is important to *stay within the lines* to meet *optical scanning requirements.*

Block 1. Agency Use Only *(Leave blank)*.

Block 2. Report Date. Full publication date including day, month, and year, if available (e.g. 1 Jan 88). Must cite at least the year.

Block 3. Type of Report and Dates Covered. State whether report is interim, final, etc. If applicable, enter inclusive report dates (e.g. 10 Jun 87 - 30 Jun 88).

Block 4. Title and Subtitle. A title is taken from the part of the report that provides the most meaningful and complete information. When a report is prepared in more than one volume, repeat the primary title, add volume number, and include subtitle for the specific volume. On classified documents enter the title classification in parentheses.

Block 5. Funding Numbers. To include contract and grant numbers; may include program element number(s), project number(s), task number(s), and work unit number(s). Use the following labels:

C	- Contract	PR	- Project
G	- Grant	TA	- Task
PE	- Program Element	WU	- Work Unit Accession No.

Block 6. Author(s). Name(s) of person(s) responsible for writing the report, performing the research, or credited with the content of the report. If editor or compiler, this should follow the name(s).

Block 7. Performing Organization Name(s) and Address(es). Self-explanatory.

Block 8. Performing Organization Report Number. Enter the unique alphanumeric report number(s) assigned by the organization performing the report.

Block 9. Sponsoring/Monitoring Agency Name(s) and Address(es). Self-explanatory.

Block 10. Sponsoring/Monitoring Agency Report Number. *(If known)*

Block 11. Supplementary Notes. Enter information not included elsewhere such as: Prepared in cooperation with...; Trans. of...; To be published in.... When a report is revised, include a statement whether the new report supersedes or supplements the older report.

Block 12a. Distribution/Availability Statement. Denotes public availability or limitations. Cite any availability to the public. Enter additional limitations or special markings in all capitals (e.g. NOFORN, REL, ITAR).

DOD	- See DoDD 5230.24, "Distribution Statements on Technical Documents."
DOE	- See authorities.
NASA	- See Handbook NHB 2200.2.
NTIS	- Leave blank.

Block 12b. Distribution Code.

DOD	- Leave blank.
DOE	- Enter DOE distribution categories from the Standard Distribution for Unclassified Scientific and Technical Reports.
NASA	- Leave blank.
NTIS	- Leave blank.

Block 13. Abstract. Include a brief *(Maximum 200 words)* factual summary of the most significant information contained in the report.

Block 14. Subject Terms. Keywords or phrases identifying major subjects in the report.

Block 15. Number of Pages. Enter the total number of pages.

Block 16. Price Code. Enter appropriate price code *(NTIS only)*.

Blocks 17. - 19. Security Classifications. Self-explanatory. Enter U.S. Security Classification in accordance with U.S. Security Regulations (i.e., UNCLASSIFIED). If form contains classified information, stamp classification on the top and bottom of the page.

Block 20. Limitation of Abstract. This block must be completed to assign a limitation to the abstract. Enter either UL (unlimited) or SAR (same as report). An entry in this block is necessary if the abstract is to be limited. If blank, the abstract is assumed to be unlimited.

CONTENTS

GENERAL INTRODUCTION

This final report describes the conclusion of the research in the Materials Group, Cambridge University Engineering Department (U.K.) and at "Demokritos" National Centre for Scientific Research (Greece), on the micromechanics of fracture of ceramic matrix composites. The first part of the report describes the continuation of a test series which has been undertaken on the laminated CAS–glass SiC fibre reinforced material provided by the USAF Materials Laboratory, Dayton, Ohio. Fracture mechanisms have been studied in four–point bend and in two new geometries – double cantilever beam and double edge–notched tension. Dynamic in–situ scanning electron microscopy has enabled a clear characterisation of sub–critical damage, and crack interactions prior to final failure, both of which have a strong influence on the material failure strength.

The second part of the report describes preliminary studies on the fracture behaviour of alumina toughened with ductile metal reinforcements. Specimens of alumina reinforced with discrete particles (mainly cobalt) have been produced by pretreating metal powders and mixing them with alumina powder followed by sintering under protective atmospheres. Processing conditions have been developed, and fracture surfaces studied in the scanning electron microscope. Crack bridging by metal ligaments has been observed. The ligaments fail by necking and/or shearing. The materials and processing route appear to be promising, especially in terms of controlling the interfacial reactions and strength.

ACKNOWLEDGEMENTS

We would like to thank Mr A Heaver (CUED) and Mr E Sofianopoulos ("Demokritos" NCSR) for their practical assistance in this work. The financial support of the U.S. Air Force Office of Scientific Research through grant no. AFOSR–87–0307 is gratefully acknowledged.

A. CAS–GLASS SiC FIBRE COMPOSITES

1. INTRODUCTION

1.1 Literature survey

In recent years a number of research programmes have been undertaken to investigate many aspects of processing and mechanical performance of the new generation of ceramic matrix composites. An extensive body of work has been carried out over a 5 year period at the University of California at Santa Barbara, as part of a University Research Initiative. This programme has been the source of many of the ideas pursued in this project. The results of this and other work in the literature are reviewed here, to identify the issues which could be specifically addressed using the in–situ SEM facilities at Cambridge.

A number of reviews of the mechanical properties of fibre–reinforced ceramic matrix composites have been published (Prewo, 1989; Evans and Marshall, 1989; Evans, 1990). Many studies of the strength of these materials first consider unnotched tensile behaviour (static and fatigue), with uniaxial or bending geometries. Observation and modelling of the formation of matrix cracks has been extensive. Experimental methods of monitoring cracking in relation to the load–displacement behaviour include indirect techniques such as acoustic emission and edge replication microscopy (Zawada *et al.*, 1991; Harris *et al.*, 1992a,b; Sorenson *et al.*, 1992), but also direct optical or SEM observation (Marshall and Evans, 1985; Pryce and Smith, 1991; Shercliff *et al.*, 1992; Beyerle *et al.*, 1992). A critical feature of these materials which emerges from these studies is the fibre–matrix interface. Acceptable fracture behaviour is achieved with weak interfaces which promote multiple cracking and fibre pullout. The role of the interface has in itself received considerable attention both experimentally and theoretically (Thouless and Evans, 1988; Thouless *et al.*, 1989; Cao *et al.*, 1990; Rouby and Navarre, 1990; Weihs *et al.*, 1991). The study of multiple matrix cracking by

Aveston, Cooper and Kelly (1971) has been extended by a number of authors to incorporate fibre, matrix and fibre–matrix interface properties (notably Marshall, Cox and Evans, 1985; Budiansky, Hutchinson and Evans, 1986; Zok and Spearing, 1992). Recently Curtin (1991) has shown how not only matrix crack spacing, but also mechanical properties can be related to fibre and matrix properties. The importance of bridged matrix cracks in these (and other) materials has led to major new fracture mechanics computations applied to this problem (Marshall and Cox, 1987; Zok *et al.*, 1990; Cox and Marshall, 1991; Cox, 1991; Cox and Lo, 1992a,b). The models have shown that failure by propagation of a bridged mode I crack is strongly specimen–dependent, i.e. depending on the mode of loading and on the relative sizes of specimen notch, width and crack length. While mode I cracks have been observed to propagate from notches (Zok *et al.*, 1990), frequently mixed mode cracking occurs as the weak fibre–matrix interface leads to low resistance to shear loading parallel to the fibres. Tensile loading (either uniaxial or flexure) of notched material then leads to the formation of splits parallel to the fibres and tensile axis. In cross–ply materials, it is necessary to distinguish whether the specimen is edge–notched through–the–thickness (cutting all of the plies edge–on), or surface–notched through one or two plies across the whole specimen width. Tensile testing of edge–notched laminates will be considered further below, but first we consider flexure.

Flexural loading is commonplace as a means for testing the tensile response of monolithic ceramics. In a recent review Quinn and Morrell (1991) emphasise the difficulties of conducting reproducible flexure tests and of using the data for design purposes. The apparent ease of conducting flexure tests has led to a general acceptance of the method for ceramic long–fibre composites, but as pointed out emphatically by Quinn and Morrell, and also Larsen and Stuchly (1990), this is in many ways erroneous and potentially misleading. The stress state is much less uniform than in monolithic ceramics, due to sub–critical damage initiating in the tensile half of the specimen. This reduces the modulus and moves the neutral axis, making evaluation of stresses complex.

Furthermore shear or compressive failures commonly occur. Larsen and Stuchly conclude therefore that at best flexure data are comparative only, but numerically they can be misleading from the point of view of providing design data. These limitations were noted in some of the first work on SiC–reinforced ceramics (e.g Prewo, 1986) and were endorsed by our own observations reported previously (Shercliff *et al.*, 1992). Other workers have tested surface–notched specimens in four–point bending to evaluate delamination resistance in unidirectional (Bordia *et al.*, 1991) and cross–ply material (Sbaizero *et al.*, 1990). The observations are similar to our own – failure is strongly influenced by shear or compressive damage, and the results are very specimen–dependent. Nevertheless there has been a major modelling effort applied to flexure geometries (or related tensile loading of surface–notched geometries). Numerical computations have been aimed principally at predicting the R–curve response of mixed mode delamination cracks (Suo, 1990; He *et al.*, 1990; Bao *et al.*, 1991a,b; Suo *et al.*, 1991, 1992; He and Evans, 1992). Given the experimental variability of the tests, even under nominally identical conditions, the value of extensive finite element computations is perhaps questionable. However, a useful concept which emerges from the modelling is that of orthotropy rescaling. A number of computations have shown that the stress field in orthotropic solids can often be scaled approximately to an isotropic field (Suo *et al.*, 1991; Bao *et al.*, 1991b and 1992). The scaling factors are simple functions of the main elastic constants (e.g E_{11} and E_{22}). This makes mechanics solutions for common geometries reasonably tractable, and also provides simple "rules–of–thumb" for designing specimens. For example, it is noted that an orthotropic solid loaded in its stiff direction behaves like an isotropic solid scaled in length by the quantity, $(E_{22}/E_{11})^{1/4}$. Hence a strongly anisotropic material loaded in bending behaves like an isotropic beam of reduced length[1]. This is particularly relevant when considering the relative

[1] For the CAS–glass SiC material used in this study, the orthotropy rescaling parameter for unidirectional material is 0.96, that is, the material is only weakly anisotropic.

importance of shear versus bending. Some flexure experiments in the literature already use low values of span–to–depth. Orthotropy rescaling implies that the situation is even worse, with the effective length being shorter still, which will promote shear failure rather than tensile failure. The delamination geometries analysed cover a range of mixed mode loading from pure mode I to pure mode II. Delamination is predominantly a mode II or mixed mode phenomenon. From a testing point of view however the mode I double cantilever beam (DCB) specimen offers the advantage of simplicity, with the ability to observe bridging mechanisms directly due to the significant crack opening. Fibre bridging in this geometry has been modelled recently by Spearing and Evans (1992) and Kaute *et al.* (1992). While the behaviour of this specimen is in some ways academic, it should be possible to apply the information on bridging gained from in–situ DCB tests to more practical mixed mode configurations in which the crack opening is small.

The conclusion which may be drawn from the extent of flexure studies is that delamination is clearly a key issue in these materials (as in polymeric composites), but the testing to date has not been sufficiently relevant to design. The emphasis in future is likely to be more directly related to design against delamination, for example, using curved geometries or joints at which these problems arise. The tensile response of laminates with through–thickness notches is also important from the point of view of design. Mechanical joining of CMC components frequently requires the use of holes through the laminate. In a series of studies at Cambridge University the damage mechanics of notched polymeric laminates has been considered. Kortschot *et al.* (1990a,b; 1991a,b) first observed and then modelled the damage evolution from double edge–notched carbon–fibre laminates loaded in tension. The damage grew in a self–similar manner in a range of layups, and was characterised by splits from the notch root parallel to the fibres in the 0° plies with narrow 0/90 delaminations associated with each split. A predictive model for notched strength was produced. Spearing *et al.* (1992a–d) subsequently extended the models to fatigue loading, with centre–notched

specimens. The work has illustrated the notch insensitivity of CFRP, by evaluating the reduction in stress concentration at the root of a notch caused by the propagation of sub–critical damage. Further studies have tested the generality of the concepts in other polymer matrix systems (e.g. carbon–PEEK, Spearing *et al.*, 1992e; glass–epoxy and Kevlar–epoxy, Dimant *et al.*, 1992). The question therefore arises as to whether similar behaviour is found in glass SiC–fibre laminates, and other CMC systems. Some initial studies of carbon matrix SiC fibre composites have recently been reported (Heredia *et al.*, 1992), but this area has clearly received less attention than flexural testing.

1.2 Summary of research program

A review of the literature has identified the approaches which have been used to date in characterising SiC fibre reinforced ceramics. This has guided the choice of tests which have been conducted in–situ in the SEM during this project, the aim being to complement or extend previous studies. The emphasis has been on experimental observation of damage and failure mechanisms, rather than on modelling. Computations relating to the common test geometries have been extensive elsewhere, so it was considered more important to question the basis of the existing models, which in some ways have run ahead of experimental work.

The initial tests described in our previous report confirm that the CAS–glass SiC material from Dayton is essentially similar to those reported in the literature. The tensile stress–strain response shows a reduced modulus following the onset of matrix cracking, and 0^{0} ply failure occurs with extensive pullout, prompted by a weak fibre–matrix interface. The tensile unnotched response of these materials has received so much attention previously, that further tests of this type in–situ were not considered.

Flexural testing has been extensive, but is to some extent discredited due to the multiplicity of failure mechanisms and the lack of clear design information which results. A series of four–point bend tests have been continued in–situ, as the facility allows a clear picture of the damage sequence and delamination bridging which occurs. This

illustrates the difficulty, and raises the question of whether elaborate modelling of this geometry is justified.

It was noted that the double cantilever beam is a simple delamination geometry, albeit in pure mode I, as failure is by propagation of a single crack, and the large crack opening gives a clear view of the fibre bridging. DCB tests were therefore conducted in–situ.

From the design point of view, the notched tensile response is important in connection, for example, with making joints. The experience gained at Cambridge in the damage mechanics of polymeric laminates provides a sound basis for a study in this glass matrix composite. A range of tests were therefore conducted on double edge–notched specimens, to examine the development of sub–critical damage and final failure behaviour. This test series was conducted partly using conventional testing machines due to the use of both static and fatigue loading, and limitations of load levels on the in–situ facility. Tests were interrupted for SEM examination to maintain a consistent standard of observation of the behaviour as in the dynamic in–situ tests.

2. EXPERIMENTAL WORK, RESULTS AND DISCUSSION

2.1 Material

The laminated material supplied by the USAF Materials Laboratory, Dayton, consisted of various layups of CAS (calcium–alumino–silicate) glass reinforced by Nicalon SiC fibres. The properties of the fibres and matrix materials are given below. The work described in this report on new specimen geometries (double cantilever beam and double edge–notched tension) was based on a 6–ply laminate: $(0/90/0)_s$. The continuation of four–point bend tests used a 7–ply laminate: (0/90/0/90/0/90/0).

2.1.1 SiC Nicalon fibres

Nicalon fibres are manufactured by Nippon Carbon Co. by the spinning and heat treatment of an organic–silicon compound. The composition is Si–C–O (in approximate ratio 1.0:1.25:0.4, with a small H content) rather than SiC. It is composed of a mixture of β SiC microcrystallites with average diameter 4.3 nm, measured by X–ray diffraction peak–broadening (Pysher *et al.*, 1989), and an amorphous phase. It is usually supplied in tows composed of rovings of approximately 500 fibres/roving coated by various sizings depending on the application. The microcrystallite size is not observed to change after exposure to temperatures as high as 1500°C, implying good stability of fibre properties at elevated temperature. The average diameter of the filaments used in the USAF material was given as 12μm and measured as 12.5μm $\pm$ 1.5μm, though we did observe a few extreme fibres outside this range.

Some of the properties of Nicalon fibres are given in Table 1. Nicalon fibres display linear elastic behaviour until brittle fracture up to a temperature of 1200°C, above which plastic deformation occurs (Pysher *et al.*, 1989). The fracture stress obeys a Weibull distribution, governed by the statistical nature of the flaws in the fibres. The probability of failure at a given stress therefore increases wih increasing gauge length. It should therefore be noted that the stresses carried by bridging fibres (of effectively very

TABLE 1: Some properties of the Nicalon fibres
(Data supplied by Nippon Carbon Co, except * Pysher *et al.*, 1989).

Density		2.55 Mg/m^3
Thermal expansion coefficient		3.1×10^{-6} K^{-1}
Specific heat		1.14×10^3 J/kg K
Thermal conductivity		12 W/m K
Tensile strength*	20°C	1900 MPa
(standard	800°C	1900 MPa
gauge length)	1200°C	1500 MPa
	1500°C	1000 MPa
Young's modulus*	20°C	190 GPa
	800°C	175 GPa
	1200°C	125 GPa
	1500°C	90 GPa
Elongation (standard gauge length)		1.5%

short gauge length) can in principle reach values significantly higher than the average properties given for conventional test gauge lengths (Kaute *et al.*, 1992). Its Young's modulus decreases slowly with increasing temperature up to 800°C and then falls to half the room temperature value at 1500°C. The strength shows similar behaviour. The fibres are resistant to chemical attack, but oxidise slowly above 1000°C. The recent development of C–coated fibres has extended the useful temperature range to 1500°C. These fibres are thus well suited to application as reinforcement in a wide range of ceramic and metal matrices for high temperature materials.

2.1.2 CAS glass matrix

The composite matrix was an electrical type glass (Corning Glass Works, Code 1723). The composition is given in Table 2a. The average grain size was about 12μm, and typical properties are given in Table 2b. It should be noted that manufacture of the composite can lead to quite wide differences in the glass microstructure and properties.

Table 2a: Manufacturers' composition (wt%) of the CAS glass matrix

SiO_2	B_2O_3	Al_2O_3	CaO	BaO	MgO	As_2O_3
56.8	4.3	15.5	10.0	6.0	6.9	0.5

Table 2b: Some properties of the glass matrix
(from Handbook of Materials Science, 1974)

Softening point	$908^{o}C$
Working point	$1168^{o}C$
Coefficient of thermal expansion	$4.6 \times 10^{-6}\ K^{-1}$ $(0–300^{o}C)$
	$5.2 \times 10^{-6}\ K^{-1}$ $(300–665^{o}C)$
Young's modulus	86 GPa
Density	$2.64\ Mg/m^3$

2.2 Four–point bend tests

2.2.1 Summary of earlier work

In the previous report (Shercliff *et al.*, 1992) tests on 7–ply 0/90 specimens in four point bend were described. The specimen geometry is shown in Figure 1. The tests showed that the initial damage which propagates from a through–ply surface notch was broadly self–similar, but final failure occured by two widely different mechanisms. In some cases failure was shear–dominated: failure initially in the outer spans, which propagated into the central constant moment span, leading to failure in the compressive half of the specimen. In other cases tensile failure of the most heavily loaded 0^{O} ply occurred, and the location of failure was not necessarily below the notch. In all cases delaminations propagated along the first 90/0 interface below the notch, thereby diminishing the stress concentration. The delaminations ran one or two fibres below the interface in the 0^{O} ply, leading to "low–angle bridging".

In the previous tests, two notch depths were used – one specimen was cut just through the surface 0^{O} ply, another to halfway through the 90^{O} ply below. The first cracks grew down from the notch at roughly 45^{O} into the 90^{O} ply and then along or close to the next 90/0 interface. The effect of deepening the notch was therefore to shorten the length of unbridged delamination – see Figure 2. Load was transferred into the critical 0^{O} ply more effectively in the second case, and delamination better resisted by the longer bridging zone. This second case was one in which catastrophic shear failure in the outer span was avoided and tensile failure occurred in the critical 0^{O} ply. It would therefore seem that the notch depth can have a critical influence on the extent of delamination bridging, and the subsequent failure mode in four point bend tests of cross–ply material. Note that in unidirectional material, often reported in the literature, this effect is absent as the root of the notch always lies in a 0^{O} ply.

A second major influence on the damage mechanism and failure behaviour is the statistical fluctuation in fibre distribution (waviness). This affects the extent of

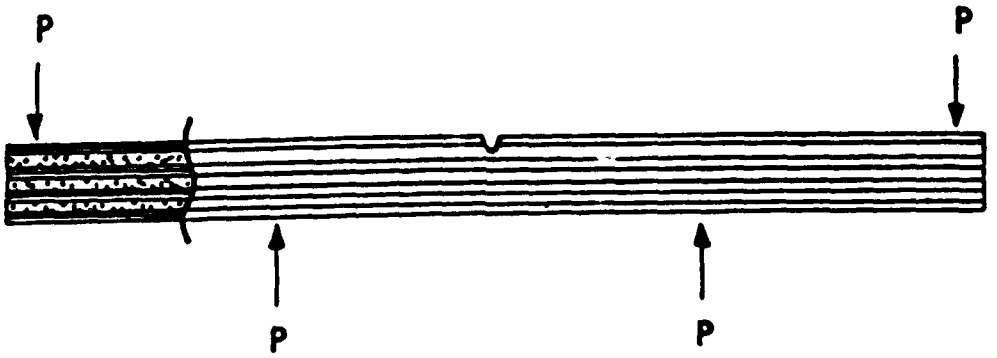

FIG.1 – Schematic of the four–point bend specimen.

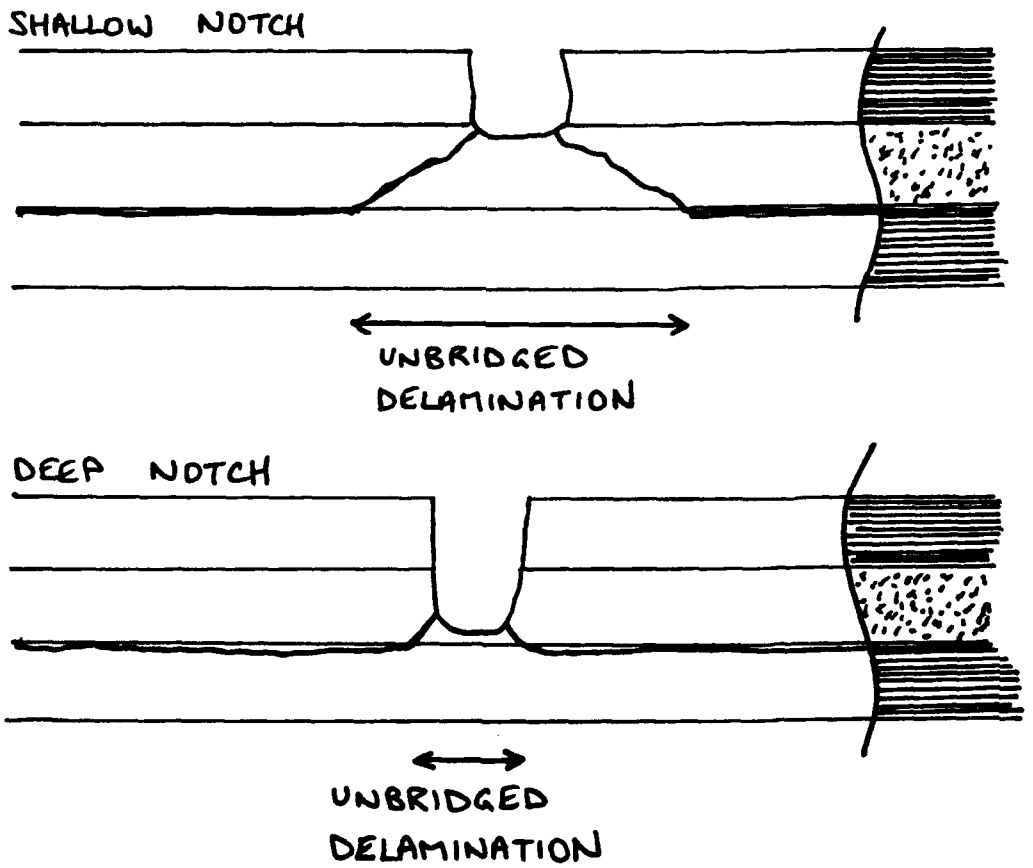

FIG.2 – Schematic of the effect of notch depth in four–point bend of cross–ply laminates on the initial damage and length of unbridged delamination.

delamination bridging, and the symmetry of the damage to either side of the notch. In cases of tensile failure, the location of the failure is further influenced by the Weibull variability of fibre strength – failure is not necessarily below the notch, even though the stress concentration is still highest there. The load–deflection response and maximum bending moment at failure was therefore subject to wide variation, even within a single failure mode.

Similar tests by Bordia *et al.* (1991) and Sbaizero *et al.* (1990) not conducted in–situ, have identified the onset of tensile, compressive and shear damage coupled to kinks in the load–displacement response. As their tests use a different span–to–depth ratio, and different inner–to–outer span ratio, the relative magnitudes of shear and bending stresses are different. Consequently the damage sequence observed differs from that observed in our in–situ tests.

It was noted in section 1.1 that four–point bend data is very specimen dependent and of limited merit. It is apparent that the variability arises from: (a) the statistical variation in fibre strength and packing; (b) variations in notch depth leading to different damage and fibre bridging; (c) variations in ratios of specimen dimensions changing the relative importance of shear, compression and tensile stress on the damage and failure mechanisms. Studies using this geometry really need to be conducted over a wider range of loading combinations, with duplicate tests of nominally identical loading. Limits on quantities of material generally make this impossible. In our own test program using in–situ rigs, space restriction in the SEM does not allow a wide variation in the four point bend configuration. Two further four–point tests were conducted in–situ using the same specimen geometry to those described in the previous report, but with deeper notches with the intention of promoting delamination bridging and tensile failure. The results are discussed below.

2.2.2 Further observations

In the first test, the notch was cut through two plies to the 90/0 interface. The delamination which formed at a low load thus extended right to the notch root, and was effectively fully bridged (Fig.3a). A crack still formed in the 90^{0} ply at a low angle to the delamination (Fig.3b). As in an earlier test tensile failure occurred close to the notch, observations were made in this region. However in this test failure occurred roughly halfway between the notch and the inner loading point, and it was also found that the 90^{0} ply nearest the compressive face had failed in shear, probably as the load redistributed after tensile failure (Fig.4). Dynamic observation of failure was not therefore made, which illustrates one of the difficulties of in–situ testing where failure can occur in many locations. The test supported the hypothesis that a notch which produced a fully bridged delamination was more likely to lead to tensile failure, but did not lead to any new dynamic observations of fracture.

The aim of the last test was to replicate the measurements of Bordia *et al.* (1991), by measuring delamination crack length to calculate the R–curve for delamination toughness. Crack tips could be located with more precision using the in–situ rigs, though it was somewhat laborious moving the stage around to locate the two crack tips of this geometry. The notch was cut through 1.75 plies, to encourage tensile failure and give the maximum length of valid crack growth. The test behaved as expected initially, though it was clear that the delamination crack was growing more easily to one side of the notch as the surface plies displaced further on one side (Fig.5a). It was found that the crack to the left of the notch rapidly reached the inner loading point, so only a few measurements of total crack length were possible, and these were of little value as the damage was so asymmetric. It was therefore difficult to measure an R–curve for delamination in this geometry, but as the damage is not reproducible this would be of limited value anyway. Bordia *et al.* also found large variations in the R–curves measured on a number of similar specimens. Failure consisted of the surface plies to the left of the notch peeling back completely, as shown in Figs.5b–d. The

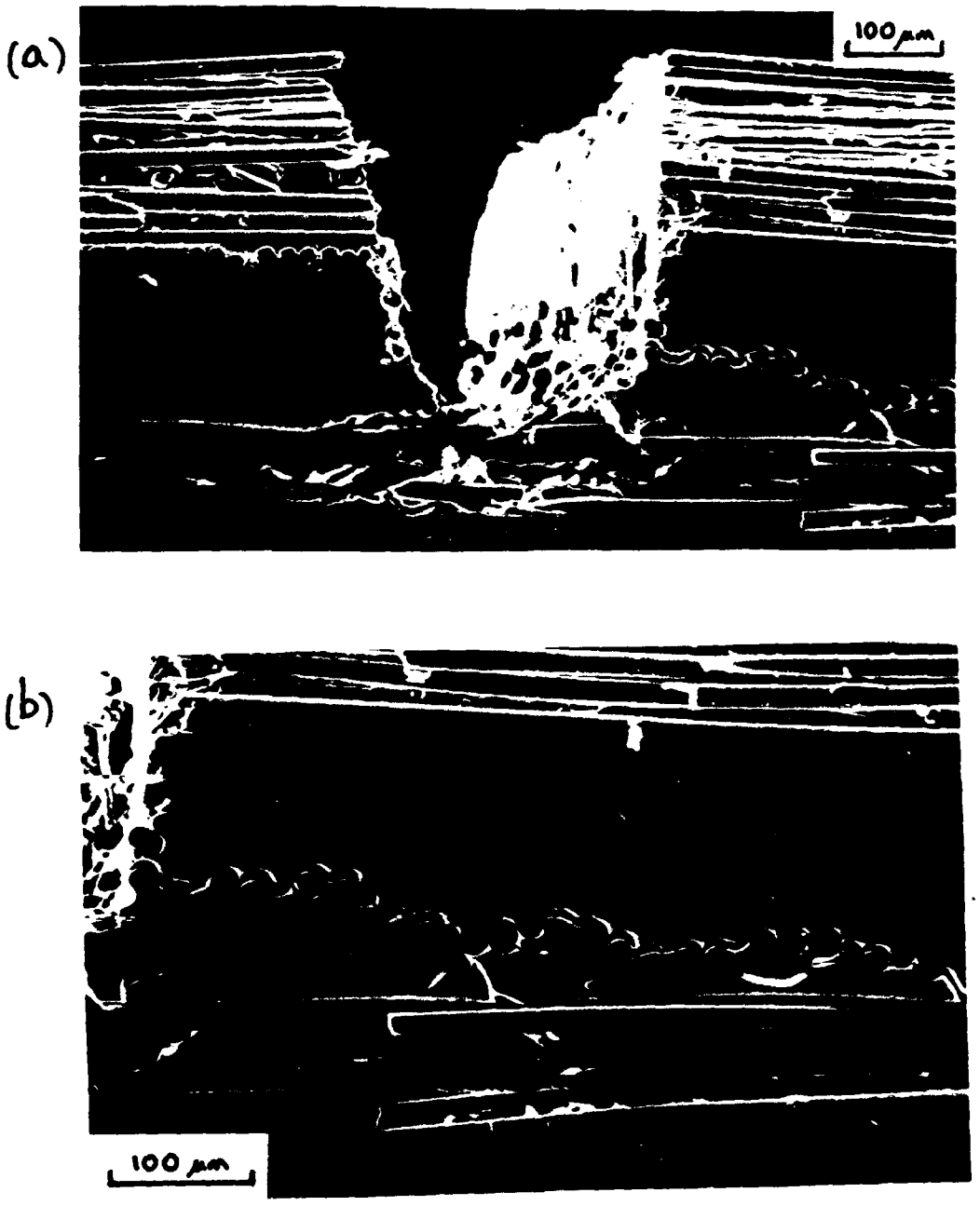

FIG.3 – SEM micrographs showing development of damage from the notch root in four–point bend test in 7–ply (0/90) CAS–glass/SiC material.

FIG.4 – SEM micrograph of shear failure in 90^{o} ply nearest compressive face of four–point bend specimen.

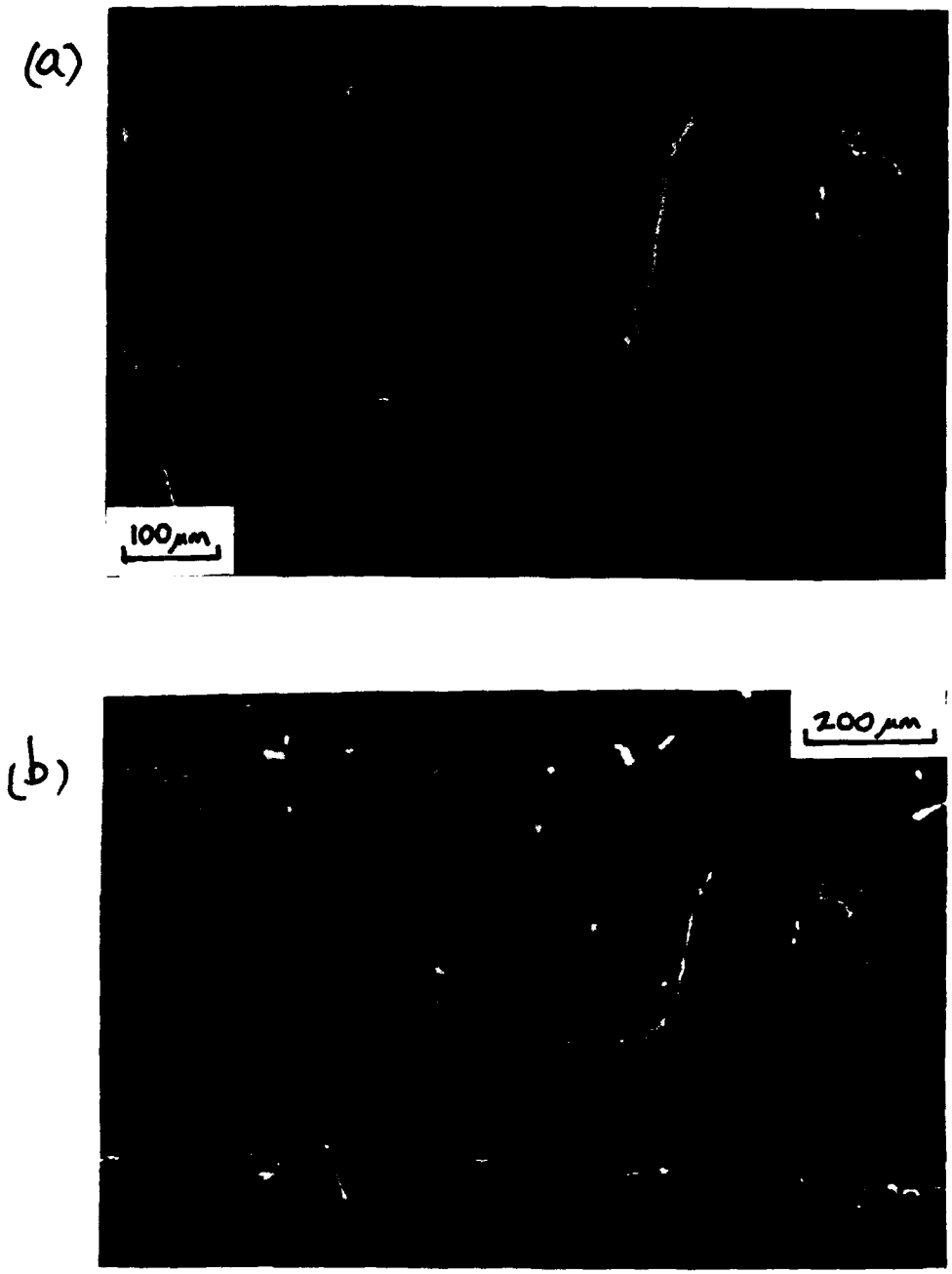

FIG.5 – SEM micrograph showing asymmetric failure by delamination in four–point bend specimen.

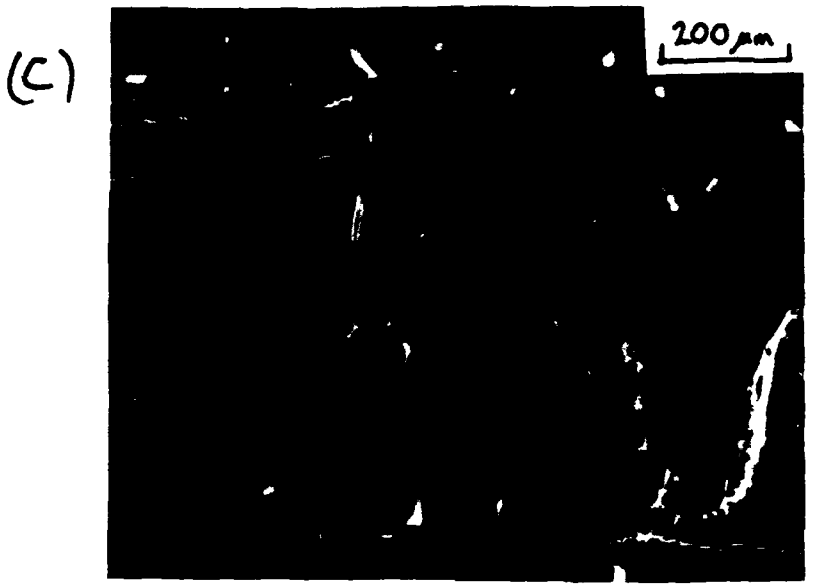

FIG.5 (Continued)

fluctuations in fibre waviness can therefore lead to very marked asymmetry in the damage. Hence while delamination bridging and tensile failure are promoted by locating the notch root near a 90/0 interface, this mechanism cannot be guaranteed as the statistics of fibre layout are even more important.

2.2.3 Summary and conclusions

The additional four–point bend test partially confirmed the earlier observations on the effect of notch depth, but produced an even greater lack of symmetry and reproducibilty than before. The damage is influenced not only by notch depth and specimen dimensions, but also by the variability in fibre waviness. The problems with using this test geometry are therefore underlined. It is also clear that there is little justification for extravagant modelling of, for example, bridging of the delaminations which propagate in notched four–point bend tests, as the damage is not experimentally reproducible. The next test series used a simpler geometry to try and overcome some of the limitations of the four–point bend configuration.

2.3 Double cantilever beam tests.

The difficulty of measuring a delamination R–curve in the four–point bend geometry suggests the use of a different geometry to assess the resistance of the material to delamination. The double cantilever beam (DCB) has the advantages of simplicity, with a single crack tip, and a crack path embedded in a 0^{o} ply. The loading is however mode I, whereas practical delaminations are essentially mode II, with possibly a partial mode I component. However, it is of value to conduct DCB tests in–situ as a clear interpretation of mode I fibre bridging can be obtained, due to the large crack opening, and some of this information is of value in understanding mode II delamination, when the crack remains closed and direct observation is precluded.

2.3.1 **Experimental observations: $(0/90/0)_s$**

The double cantilever beam geometry used is illustrated in Figure 6. Specimen dimensions were approximately 27×10×1.5mm. Load was applied via pinned grips glued to the specimen surfaces. The $(0/90/0)_s$ layup provides a double central ply in which a 0.15 mm notch could be cut. At a small load, a crack initiated near the notch root and propagated parallel to the fibres in the double 0^{o} ply (Fig.7a). The crack ran down the centre of the ply, and as the crack opening increased bridging fibres could be seen, spanning the crack at a low angle (Fig.7b). A single fibre provides both mode I and mode II tractions to the crack face, but as fibres bridged in both directions, overall the mode II components would approximately balance. The bridging persisted to large crack openings with the main features being: (a) the fibres were very straight, thus apparently carrying considerable tensile forces (Figs.7c,d); (b) fibres failed intermittently, always close to the point where they emerged from the crack flanks, with the density of bridging fibres thus falling steadily with increasing crack opening behind the crack tip; (c) the maximum angle of the bridging fibres remained below approximately 15^{o}, that is as the crack opened, the spacing of the points on the crack faces at which the fibre emerged also increased (by breaking off chips of matrix

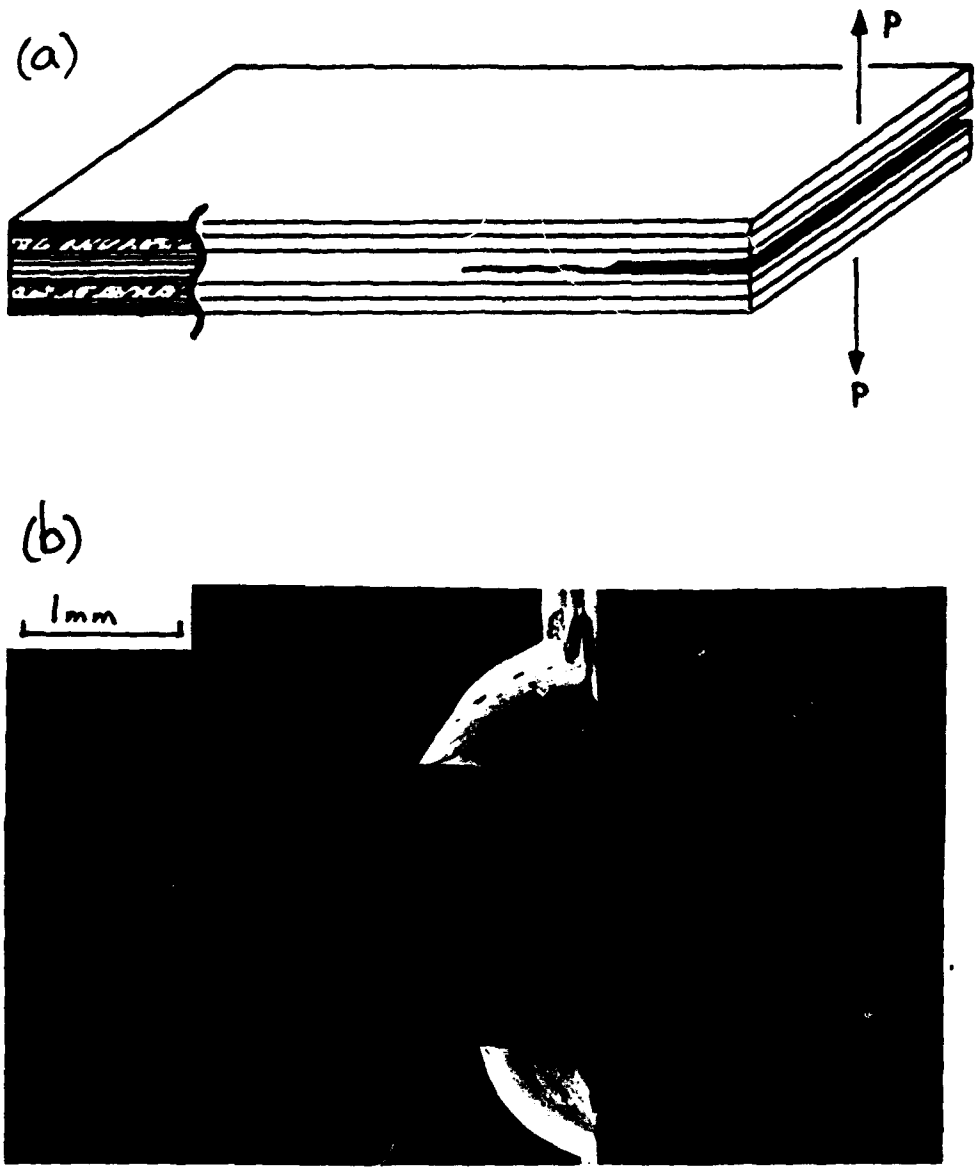

FIG.6 – The double cantilever beam specimen in (0/90/0)s CAS–glass/SiC: (a) schematic; (b) SEM micrograph of starter notch in central double ply.

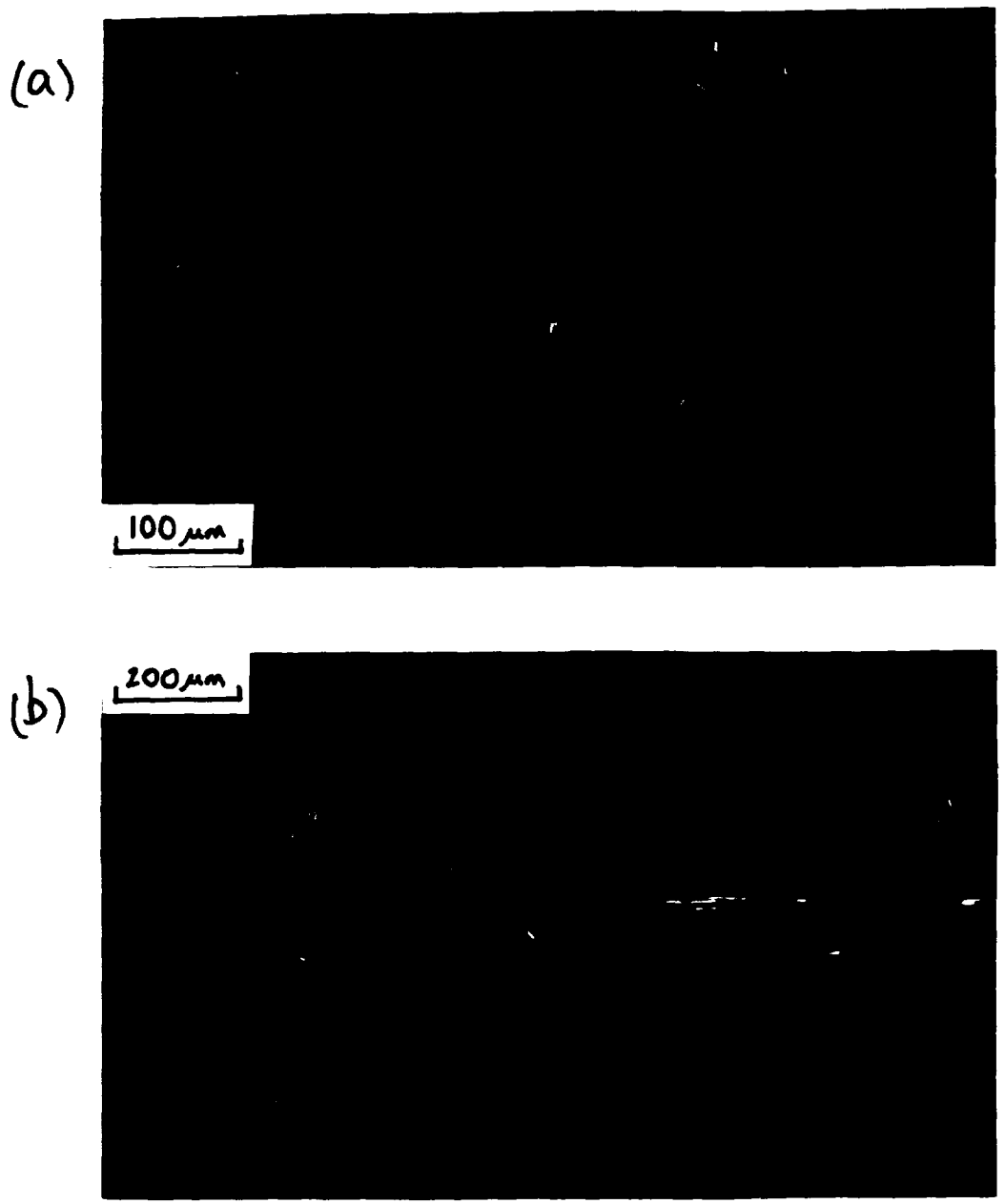

FIG.7 – SEM micrographs of the development of the crack in a DCB test on (0/90/0)s material: (a) initial crack from notch; (b) low angle bridging by single fibres.

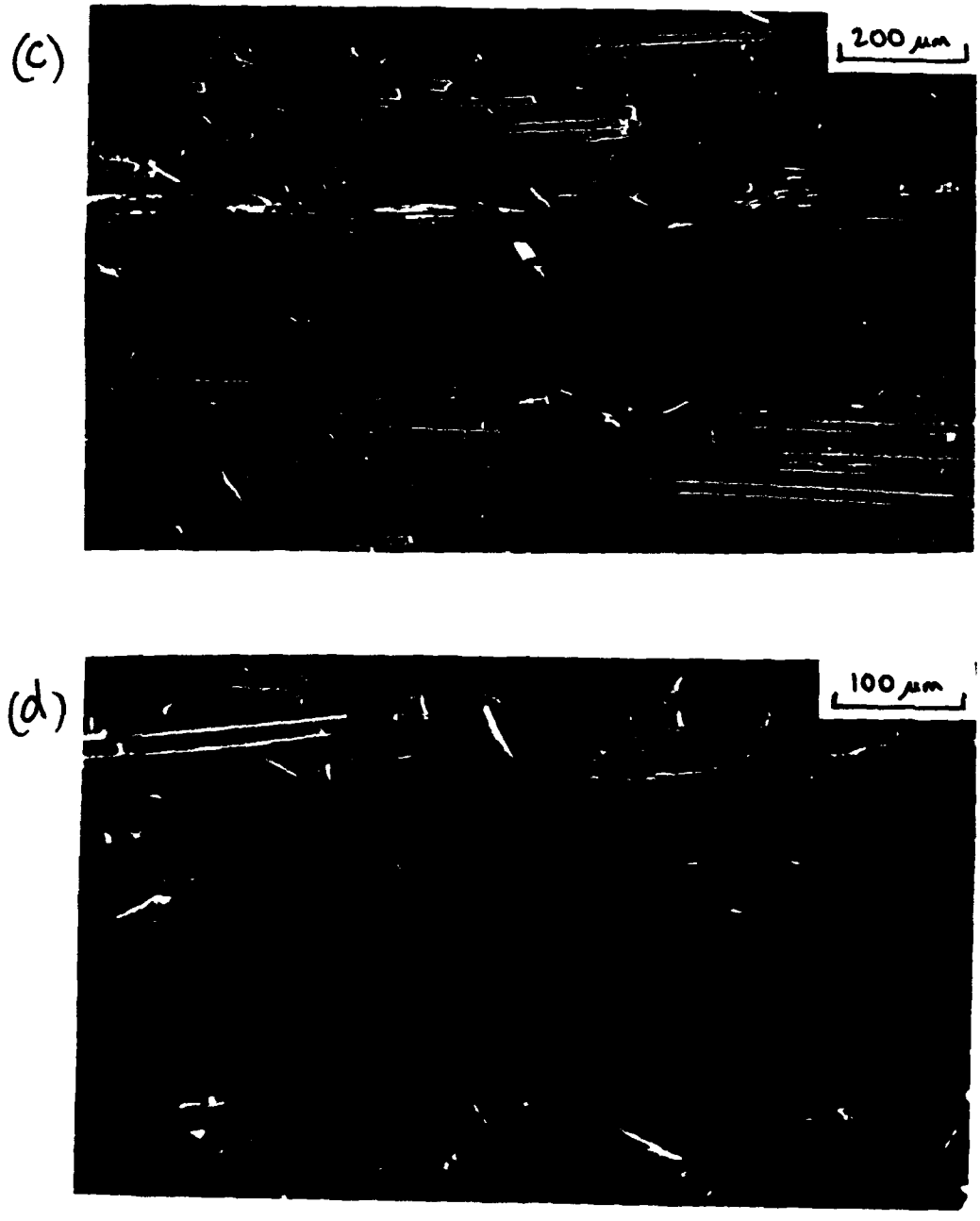

FIG.7 (Continued)
(c,d) multiple low angle fibre bridging at large crack opening, showing straightness of fibres.

(e)

(f)

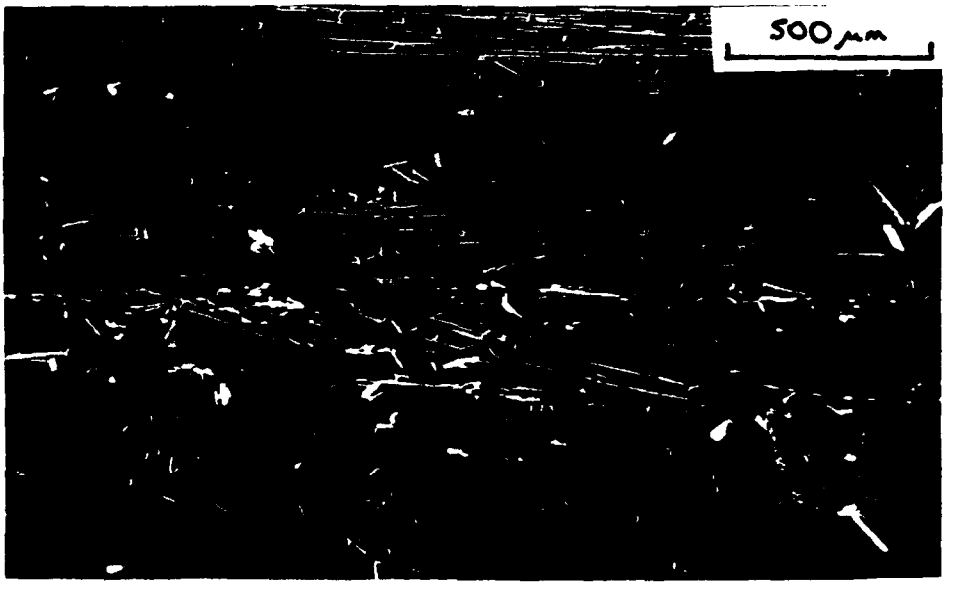

FIG.7 (Continued)
(e) an isolated bridging fibre at a large angle compared to the other bridging fibres.
(f) a bundle of fibres bridging the crack in the same direction.

material). An exception to (c) above is illustrated in Fig.7e, where a fibre lies at roughly 45^{o}. However this fibre is clearly less taut than the others, having distinct curvature. This fibre has either broken in the matrix and pulled out, or it has debonded back to a free surface from which it has then been able to pull in. A second mode of bridging was occasionally observed – collections of fibres all bridging in the same direction (Fig.7f). These bundles started as short beams with a depth of several fibres. As the crack opened the matrix broke away, leaving individual fibres acting singly, though with a net mode II action as well as the closing mode I behaviour.

Throughout the tests, load was measured for a number of crack lengths. As the crack advanced stably, it was anticipated that the toughness was increasing with crack length (i.e. R–curve behaviour). This is because the strain energy release rate increases with crack length in this geometry, so a material of constant toughness would fail catastrophically at constant load. The test was continued until the crack reached the back face of the specimen (Fig.8a). At this time there were no fibres bridging at the notch root (Fig.8b), but the presence of the notch allowed fibres to break free more easily than those along the crack flanks in the bulk of the specimen. Hence a longer specimen would be required to develop a steady state bridging zone, which is therefore in excess of around 20mm. The critical crack opening for fibre failure can be as great as 1–2mm (Fig.8b). Clearly from a design point of view, these dimensions are excessive and so the steady–state mode I toughness is of little importance in this geometry.

2.3.2 Experimental observations: $(90/0/90)_s$

A single test was carried out with the laminate rotated through 90^{o}, so the central double ply was a transverse 90^{o} ply (Fig.9a). The notch was cut below one of the 0^{o} plies so that the crack would run along the 0/90 interface – similar to the cracks in the four–pont bend tests, but with a single crack tip. The small offset of the crack from the central axis of the specimen results in mixed mode I/II loading. The crack initially appeared to run in the transverse ply at a depth of one or two fibres from the

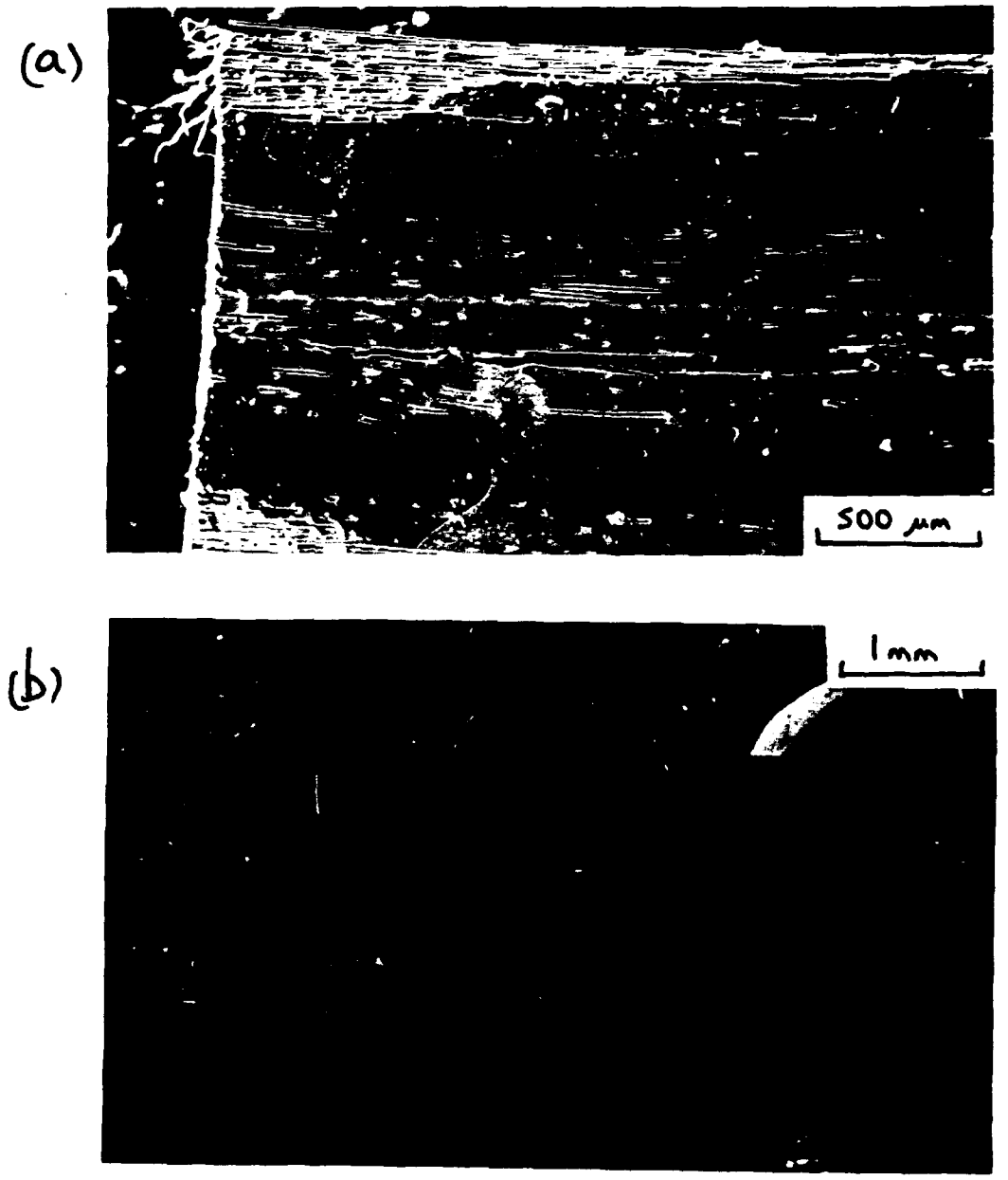

FIG.8 – SEM micrographs of the end of a DCB test: (a) crack reaching the back face of the specimen; (b) large crack opening at the notch root, showing persistent fibre bridging.

interface, largely following fibre–matrix interface (Fig.9b). Secondary cracks formed in the transverse ply, behind the crack tip. Figure 9c shows a typical transverse ply crack produced by the tensile stresses acting along the top surface of the bending beam. Once the crack opening was sufficient, bridging fibres were revealed but the fibres were 0^{o} fibres in the direction of crack propagation (Fig.9d). Hence in the bulk of the specimen the crack was running a few fibres above the 0/90 interface, and the path of the cracks observed initially, in the 90^{o} ply, was only a surface effect. The delamination crack therefore behaved exactly as those in four–point bend, running in the 0^{o} ply a few fibres from the interface, with the development of low–angle bridging. As loading continued, the crack propagated along the specimen, but further cracks also formed in the 0^{o} ply, in some instances propagating back towards the notch. The delamination was not therefore a well–characterised single crack with bridging fibres, but had a more complex structure of multiple cracks and fibre bundles (Fig.9e).

2.3.3 Results and conclusions

For the $(0/90/0)_s$ tests, the toughness G_{Ic} as a function of crack length (the R–curve) was evaluated using a standard formula for this geometry (e.g. Hashemi *et al.*, 1991; Suo *et al.*, 1991, 1992; Spearing and Evans, 1992):

$$G_{Ic} = \frac{12P^2a^2}{b^2h^3E} \qquad (1)$$

where P is the load, a the crack length, b and 2h the specimen width and depth, and E is Young's modulus. The value for the modulus E is taken as that of the 0^{o} plies (which dominate the bending response of the arms of the specimen), that is, 137 GPa. Figure 10 shows the R–curves for two specimens. Note that the toughness is still increasing at the limit of valid crack lengths as the specimens were too short to develop a steady–state bridging zone. The R–curve behaviour is marked, but as noted above the higher values are only obtained with unrealistically large crack lengths and crack openings. The specimens were nominally identical but there is considerable scatter,

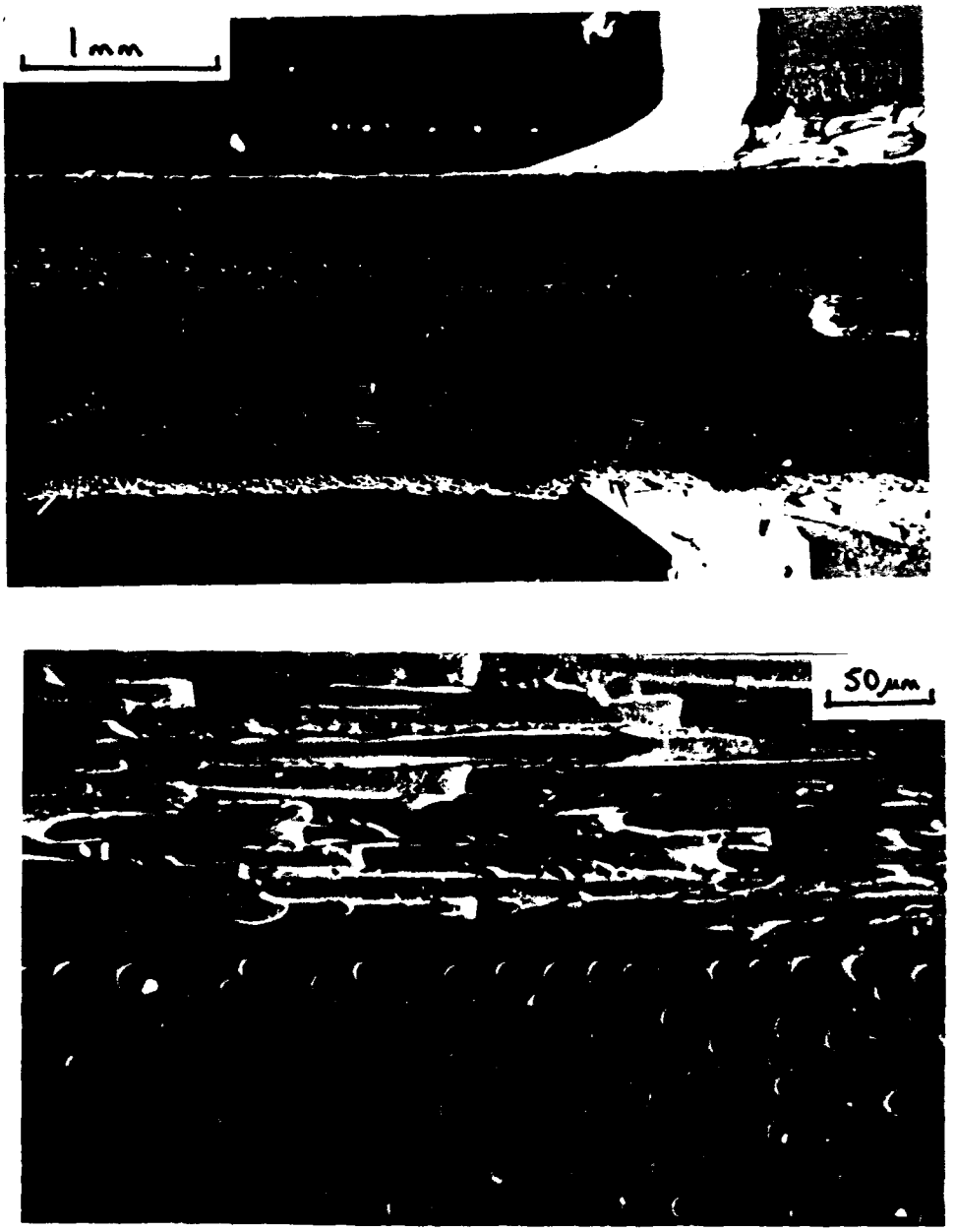

FIG.9 – SEM micrographs of DCB test on (90/0/90)s CAS–glass/SiC: (a) interlaminar crack growing from notch; (b) initial crack path in 90 ply.

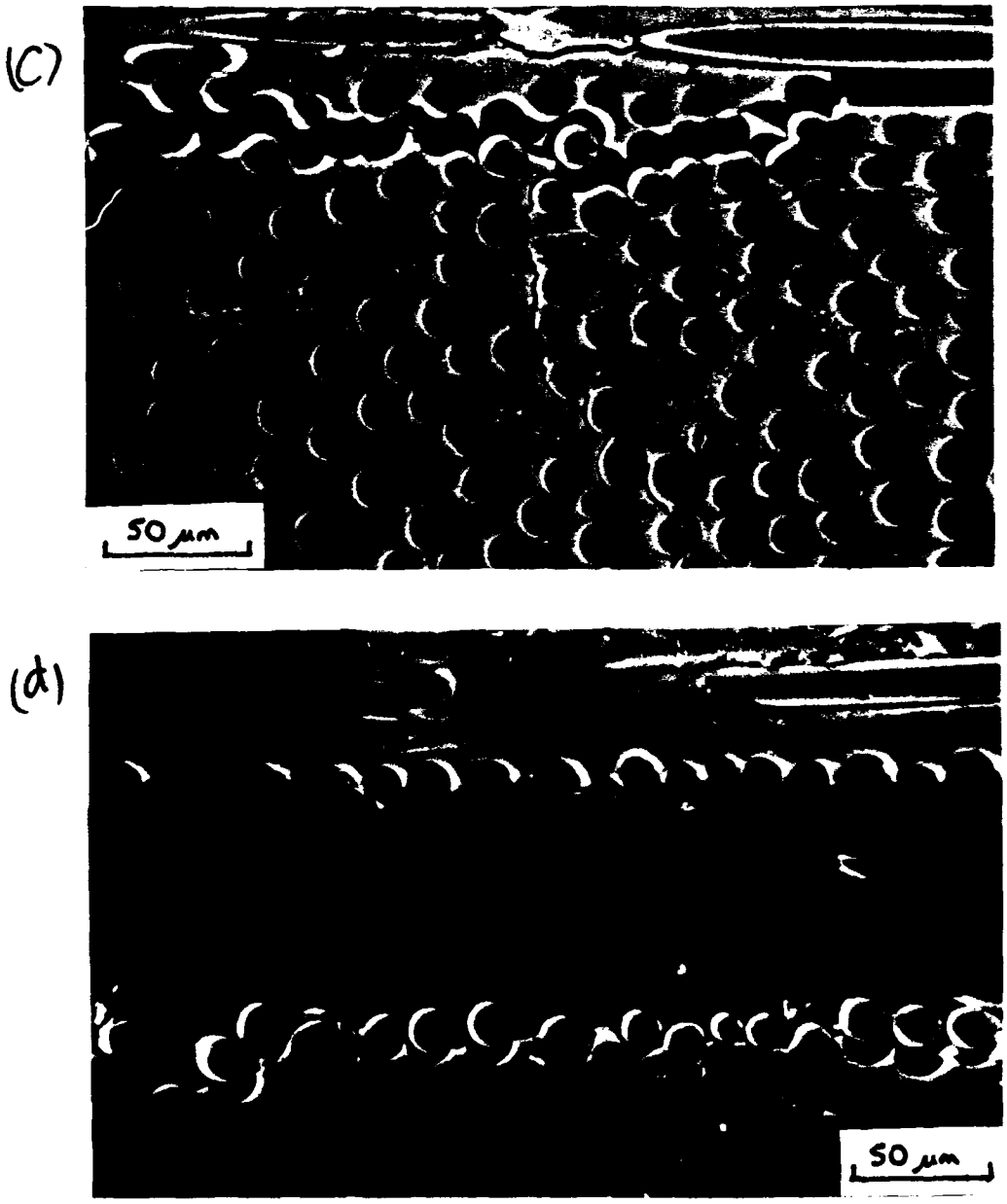

FIG.9 (Continued)
(c) transverse ply crack due to tensile stress parallel to principal crack.
(d) 0 ply bridging fibres exposed below the surface at greater crack opening.

FIG. 9 (Continued)
(e) bridged "delamination" crack within 0 ply at a later stage in the test.

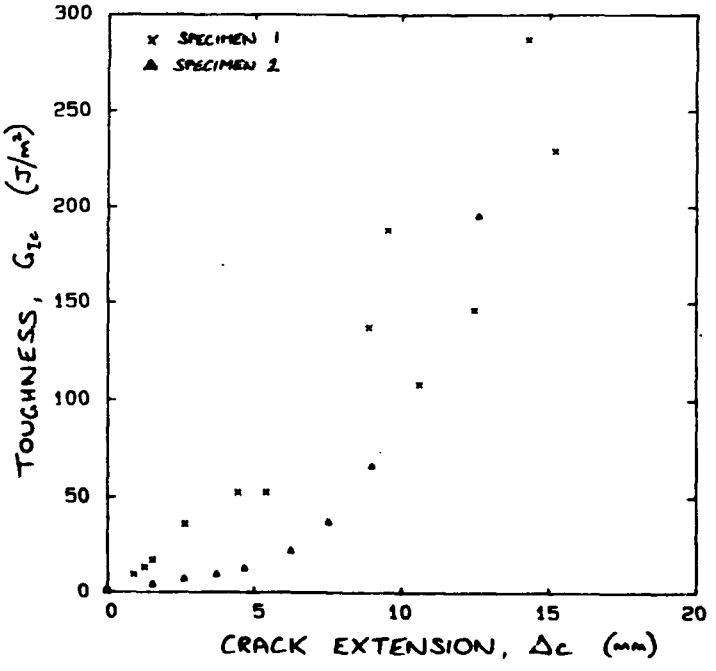

FIG.10 – Toughness against crack extension from the notch for two (0/90/0)s DCB tests, showing R–curve behaviour.

which reflects the statistical fluctuations in fibre distribution and waviness. The data are comparable to those of Spearing and Evans (1992) for tests on CAS glass–ceramic matrix material, though as they used longer specimens they reached a steady–state plateau at $G_{Ic} \cong 250$ J/m^2.

Mixed mode calibrations are available (Suo *et al.*, 1991) for double cantilever beams with offset cracks, as in the $(90/0/90)_s$ test. However, as the delamination crack produced was complex and irregular, toughness has not been evaluated from this test. Mixed mode data would be more readily obtained from unidirectional material with offset notches, as the bridging developed would be more uniform and the bending beams would not have weak transverse plies at the surface.

The marked mode I R–curve must stem from the considerable closing tractions exerted by the bridging fibres. Spearing and Evans (1992) modelled this R–curve by assuming that the bridging tractions result from fibre bending – that is the exposed fibre is effectively clamped horizontally where it emerges from the crack face, and has its ends displaced vertically as the crack opens. Our observations indicate that the fibres carry considerable tension, due to their straightness. A model for the closing traction should therefore take this into account. The magnitude of the tensile stresses in the fibres can be estimated from simple geometry. If we neglect debonding but consider the fibres pinned at the crack faces, then the strain in the exposed length of fibre is $\epsilon = (\ell - \ell_0)/\ell_0$ where ℓ is the length of exposed bridging fibre, and ℓ_0 is its original length, parallel to the crack (see Fig.11a). Substituting the fibre angle, ϕ, gives an estimate of the fibre stress:

$$\sigma = E\epsilon = E\,(\sec\phi - 1) \qquad (2)$$

Bridging angles have been measured from a number of positions along the crack, for various crack tip positions (measuring crack opening u and ℓ_0, then noting that $\tan\phi = u/\ell_0$). Figure 11b shows data for u and ℓ_0, with the corresponding angles. As noted above, the maximum bridging angle is around 15^o. Taking this value, which gives the highest stress, and a fibre modulus of 200 GPa, then the fibre stress would be 7 GPa.

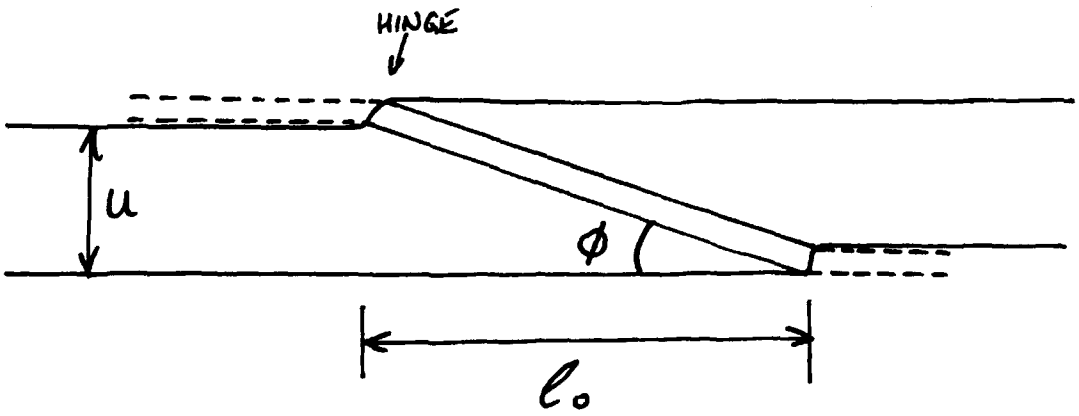

FIG.11a – Schematic of simple bridging geometry assumed for estimation of fibre tensile stresses.

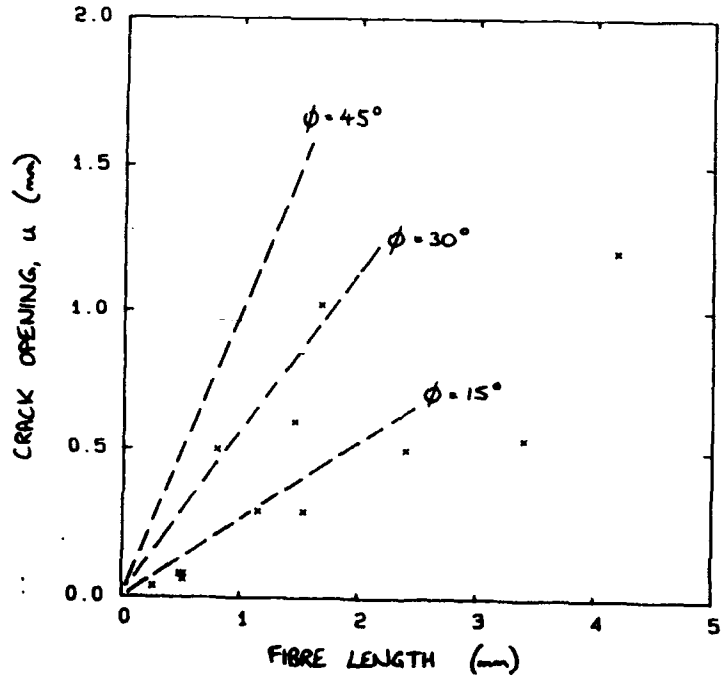

FIG.11b – Data for crack opening u and length of fibre exposed (parallel to the crack) ℓ_o, with lines of constant bridging angle ϕ.

This stress is rather high, compared to quoted tensile strengths of Nicalon fibres of 1.9 GPa. However, it should be noted that debonding will occur such that a greater length of fibre can stretch to accommodate the crack opening, reducing the stress. Furthermore, the length of fibre under load is small (of the order of 100μm – 1mm). Hence it is expected that the stress will be considerably above the quoted strengths, since the strength will follow a Weibull distribution with smaller volumes (i.e. lengths) of fibres sustaining higher stresses with the same failure probability. Fibre stresses above 2 GPa do not therefore appear unreasonable. The mode I closing traction exerted per fibre is given by $(\sigma \sin\phi)\pi d^2/4$, where d is the fibre diameter. For a diameter of 10μm, we therefore estimate the maximum closing force per fibre as being of the order of 40–100 mN. These calculations are very approximate but indicate that a full model of bridging behaviour in DCB tests should take due account of the fibre tensile stresses. Such a model has been developed recently by Kaute *et al.* (1992), using more detailed SEM observations of the same phenomena.

In conclusion, the double cantilever beam tests have shown the following:

(i) the resistance to propagation of a crack down the centre of a ply parallel to the fibres shows marked R–curve behaviour in mode I; however, the toughness develops slowly over unrealistically large crack lengths and openings.

(ii) fibres bridge the crack in both directions at an angle which mostly does not exceed 15^0; fibres fail intermittently such that the density of bridging fibres falls steadily behind the crack tip.

(iii) experimental observations and very approximate calculations indicate that the tensile stress in the bridging fibres is important – previous models regard the fibres as loaded in bending only.

(iv) the mode I observations show the geometrical configuration of fibres bridging a crack in the 0^0 ply. From this the mode II behaviour could be inferred, assuming the same fibre bridging geometry but now at zero crack opening – remote mode II loading will immediately introduce mode II closing tractions (tensile in half the fibres, and

compressive in the other half) as the faces try to slide past one another.

(v) mixed mode loading of an offset interlaminar crack revealed similar behaviour to the "delaminations" seen in four–point bend – the crack runs one or two fibres within the 0^{o} ply, and experiences low angle bridging. Initial observations erroneously indicated that the crack ran in the 90^{o} ply, but this was only a surface effect.

2.4 Double Edge–notched Tensile Tests

The specimens considered thus far have all contained notches with the notch root lying in the plane of the laminate – either through the surface plies (as in four–point bend) or into the edge of the laminate within a ply (as in the double cantilever beam). In practical situations, notches oriented normal to the laminate are of great importance – as in holes made for mechanical fasteners for example. It is often noted that a major limitation to the application of fibre composites is the problem of joining the composite parts to the rest of the structure.

Introducing notches into these materials frequently leads to the formation of sub–critical damage around the notch, which modifies the stress field and thus influences the failure strength. Analysis of multiple cracking problems of this type has led to the development of "damage mechanics" to predict failure in these materials. The growth in the application of damage mechanics to polymeric matrix fibre composites has been marked in recent years. As noted in section 1, a series of studies at Cambridge (by Kortschot, Spearing and co–workers) has established that through–thickness notches in carbon fibre–epoxy and other systems behave in a reproducible and quantifiable way in terms of: (a) the sub–critical damage that forms around edge and centre notches; (b) the influence of the damage on the static failure strength, and the subsequent variation of strength with specimen size; (c) the modification of the behaviour after fatigue loading; (d) the effect of damage on laminate stiffness; and (e) the effect of varying the layup. The first step in this work has always been to obtain a clear picture of sub–critical cracking and the "terminal damage state" at failure, before embarking on numerical modelling of the stress state in the material, as this depends critically on the damage. Figure 12 shows an X–ray micrograph of the damage which is typically observed in carbon–fibre epoxy, in this case from a centre–notch (after Spearing and Beaumont, 1992a). The damage consists of (a) splits in the 0° plies parallel to the tensile axis, initiating from the notch root; (b) delamination of the 0/90 interfaces as far as the tip of the split, at a characteristic angle which is maintained as the split grows; (c) transverse

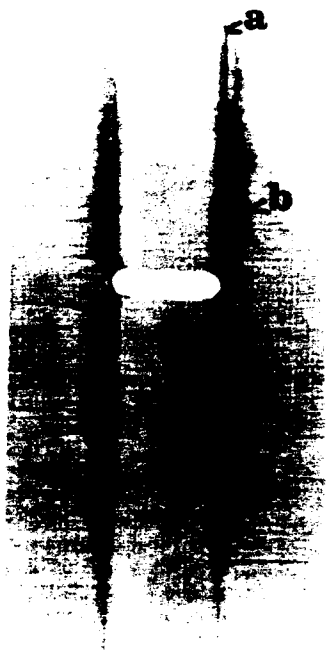

FIG.12 – A typical X–ray image of a (90/0)s CFRP centre–notched specimen (after fatigue loading) showing the damage which develops: splits (a), delaminations (b) and transverse ply cracks (c). Contrast is achieved by infiltrating the crack with ZnI_2 penetrant.

ply cracks, concentrated around the delamination zones. In general the damage shows reasonable symmetry between the four splits in a given 0^{O} ply. In static loading the damage grows with increasing stress in a self–similar manner, until the 0^{O} plies fail at the notch root. The stress concentration factor and thus failure strength could be predicted by finite element methods, taking due account of the statistical (Weibull) variation of strength of the 0^{O} plies. In fatigue the damage continues to propagate to greater split lengths than obtained in static loading. The effect of the longer splits and delaminations is to reduce the stress concentration and thereby raise the failure strength, while leading to a loss of stiffness due to the higher crack density. Implicit in this behaviour is that the material strength is not degraded by fatigue loading (e.g. by fibre failure).

A series of tests have therefore been conducted on the CAS–glass/SiC material of this study, as a preliminary assessment of the possibilities of extending this approach into ceramic matrix long–fibre laminates. Limits of material quantities and the intensive nature of the experiments have meant that the observations could not cover all of the variables mentioned above. Tests were therefore limited to a single geometry with observation of the formation of damage and final failure in static and fatigue loading, with a number of notch shapes. Observations of damage were limited to surface examination, though in principle X–radiographs could also be made of this material. This was not attempted in this project due to shortage of material – the penetrant used to infiltrate cracks for X–radiography is corrosive, so multiple specimens are required for sequential damage evaluation. Furthermore it would be best to undertake such a study on simpler laminates, such as $(0/90)_{s}$, which have fewer 0^{O} plies and 0/90 interfaces, but this layup was not available.

2.4.1 Static tests – observations of damage and failure

The first test was conducted in–situ using a double edge–notched specimen, with a V–shape notch (see Fig.13). For this and all other notched tensile tests, the laminate used was $(0/90/0)_s$, and the specimen width was between 4 and 6 mm. Load was not recorded in this preliminary test, but was measured and correlated with the damage state in subsequent tests. The ratio of total notch depth, 2a, to specimen width, w, was approximately 0.7 in this test, but was decreased to 0.5 for all subsequent tests, Figure 14a shows the view obtained in–situ, looking straight in to the V–notch. The base of the notch is not a clean V as the notch was cut by two separate angled cuts, the second of which damaged the face of the first cut. The cut faces were also quite rough as the fibres were being cut at roughly 45°, and the plies were initially difficult to distinguish from one another until some damage formed. Figure 14b shows the first cracks observed – delaminations along the 0/90 interfaces, some of which deviate into the 90° plies forming transverse ply cracks (TPCs). The density of TPCs is lower than is observed in polymeric systems. The damage is somewhat asymmetrical with longer cracks to the right of the notch. Closer inspection also revealed matrix cracks at the notch root (Fig.14c). As the load was increased the delaminations extended, further TPCs formed, and cracks formed in the 0° ply at the notch root (Fig.14d). The 0° ply cracks are shown in more detail in Figure 14e. By analogy with polymeric systems, it was assumed that these were the ends of splits running parallel to the fibres from the notch, and this was verified when the surface of the laminate was also observed in subsequent tests. The delaminations in polymeric systems extend predominantly away from the notch into the more heavily loaded ligaments of the specimen (i.e. towards the specimen edge in Fig.12). In double edge–notched specimens therefore we would expect the delaminations to grow towards the specimen centre rather than the edge (as observed by Kortschot and Beaumont, 1990a, in DEN specimens of CFRP). Without X–radiographs it is not possible to determine the extent of delamination in the central ligament, but this material appears to have a stronger tendency to delaminate out to the free edge of the

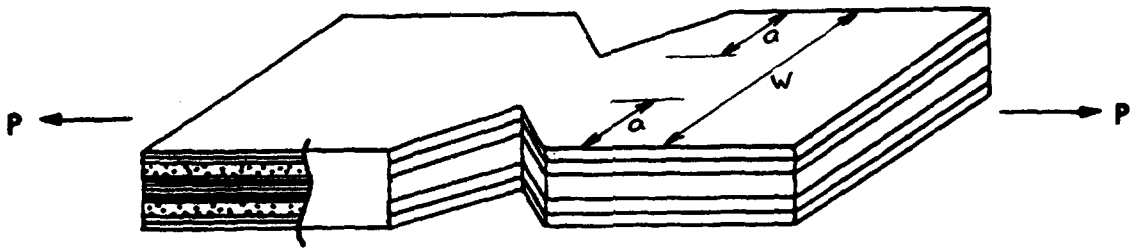

FIG.13 – Schematic of double edge–notched tensile specimen.

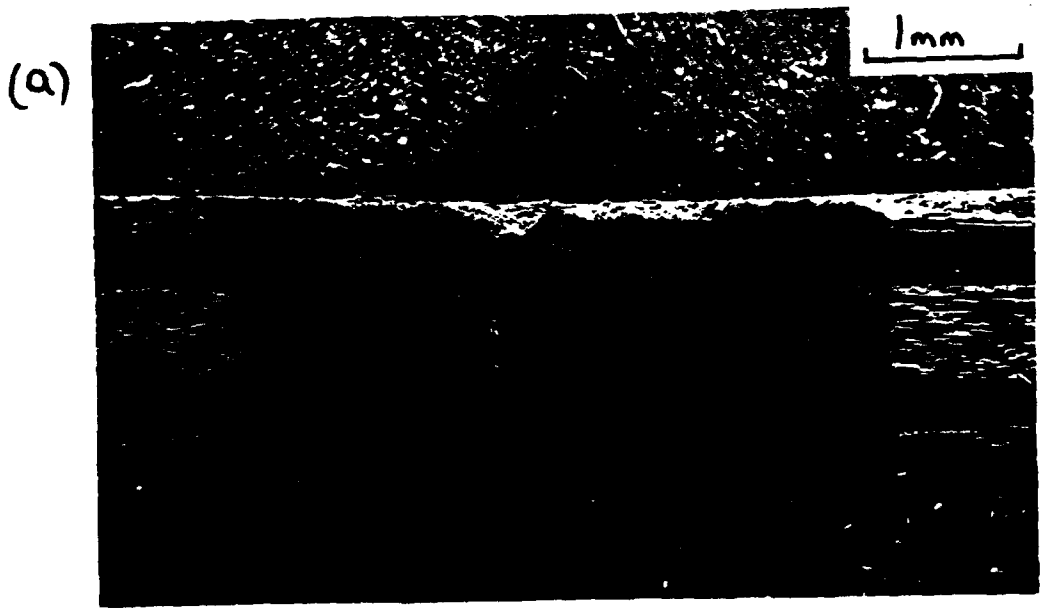

FIG.14 – SEM micrographs of the damage formed in the notch of a DEN test in (0/90/0)s CAS–glass/SiC: (a) overall view of the notch.

FIG.14 (Continued)
(b) formation of delaminations and transverse ply cracks.
(c) matrix cracks in the notch root.

FIG.14 (Continued)
(d) delaminations, splits and TPCs in the top 0/90 plies at higher load.
(e) detail of splits at notch root in 0 ply.

specimen. For a more direct comparison with the CFRP work, the notch depth was reduced to $2a/w = 0.5$ in subsequent tests.

When the damage state was as shown in Figure 14b, catastrophic failure occurred – see Fig.15a. Failure caused the damage to propagate further. Figure 15b shows the notch region at failure in more detail – note that the transverse ply cracks which opened up at failure were not at the root, and that the 0^0 fibres have also failed away from the root. Subsequent loading was required at a finite level (well below the failure load) to pull out the broken 0^0 fibres, which failed at a wide range of lengths (Fig.15c). Even after considerable separation of the grips, many 0^0 fibres still bridged the fracture (Fig.15d). Examination of the broken halves of the specimen confirmed that pullout was extensive (Fig.16a,b). The double inner plies failed more by bundle failure than by single fibre failure, but as a bundle protrudes on both fracture surfaces the location of failure was not at the notch root, and one ply failed on each side of the notch. The bundles and individual fibres show pullout lengths in excess of 1mm. Most of the failed fibres showed a clean fibre–matrix interface, with small fragments of glass adhering (Fig.17a). The transverse ply crack which opened up at failure, away from the notch root, also showed fibre bridging similar to the low angle bridging observed in the earlier test series. The waviness of the fibres which leads to this behaviour is evident on the fracture surface (Fig.17b).

To sum up the observations of this static tensile test:

(a) delaminations and transverse ply cracks form, accompanied by splits in the 0^0 plies;

(b) the damage can be somewhat asymmetrical;

(c) at a particular damage state, catastrophic failure occurs;

(d) the failure is not concentrated at the root of the notch, but is diffused through a considerable volume of material to either side, leading to extensive fibre pullout and energy dissipation.

The behaviour in (a)–(c) thus mirrors that observed in polymeric systems, but the failure process deviates. Carbon fibre–epoxy laminates always fail at the notch root.

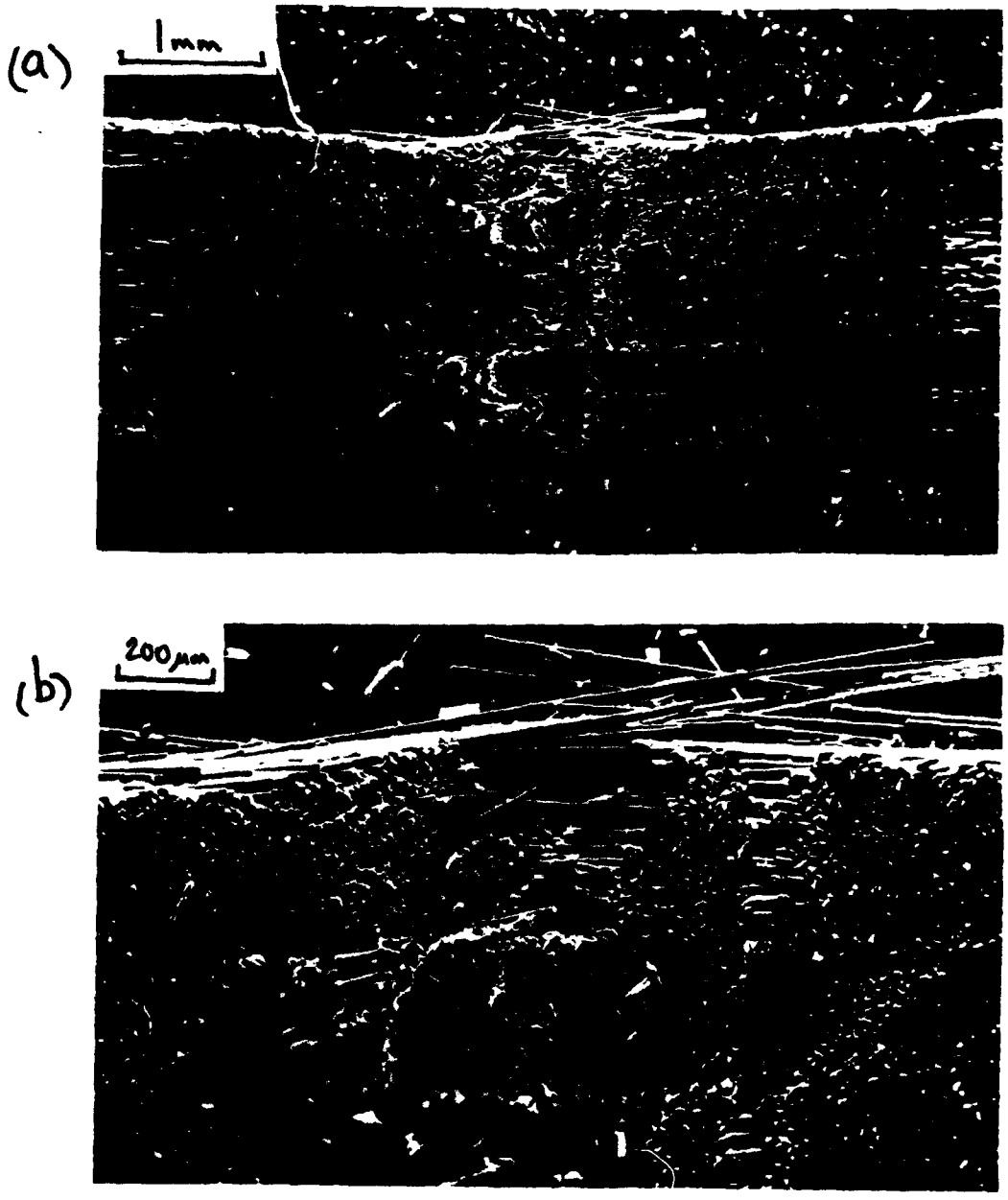

FIG.15 – SEM micrographs of failure in a DEN test:
(a) view of whole notch region immediately after failure.
(b) detail of top 0/90 plies.

(c)

(d)

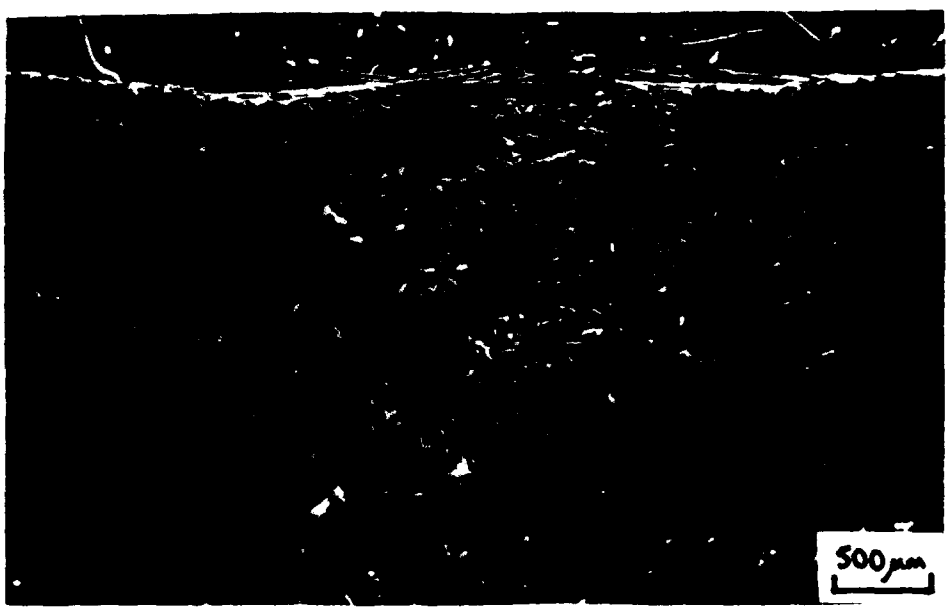

FIG.15 (Continued)
(c) fibre pullout in failed 0 ply.
(d) view of whole notch region after extensive pullout, with some 0 fibres still bridging the fracture.

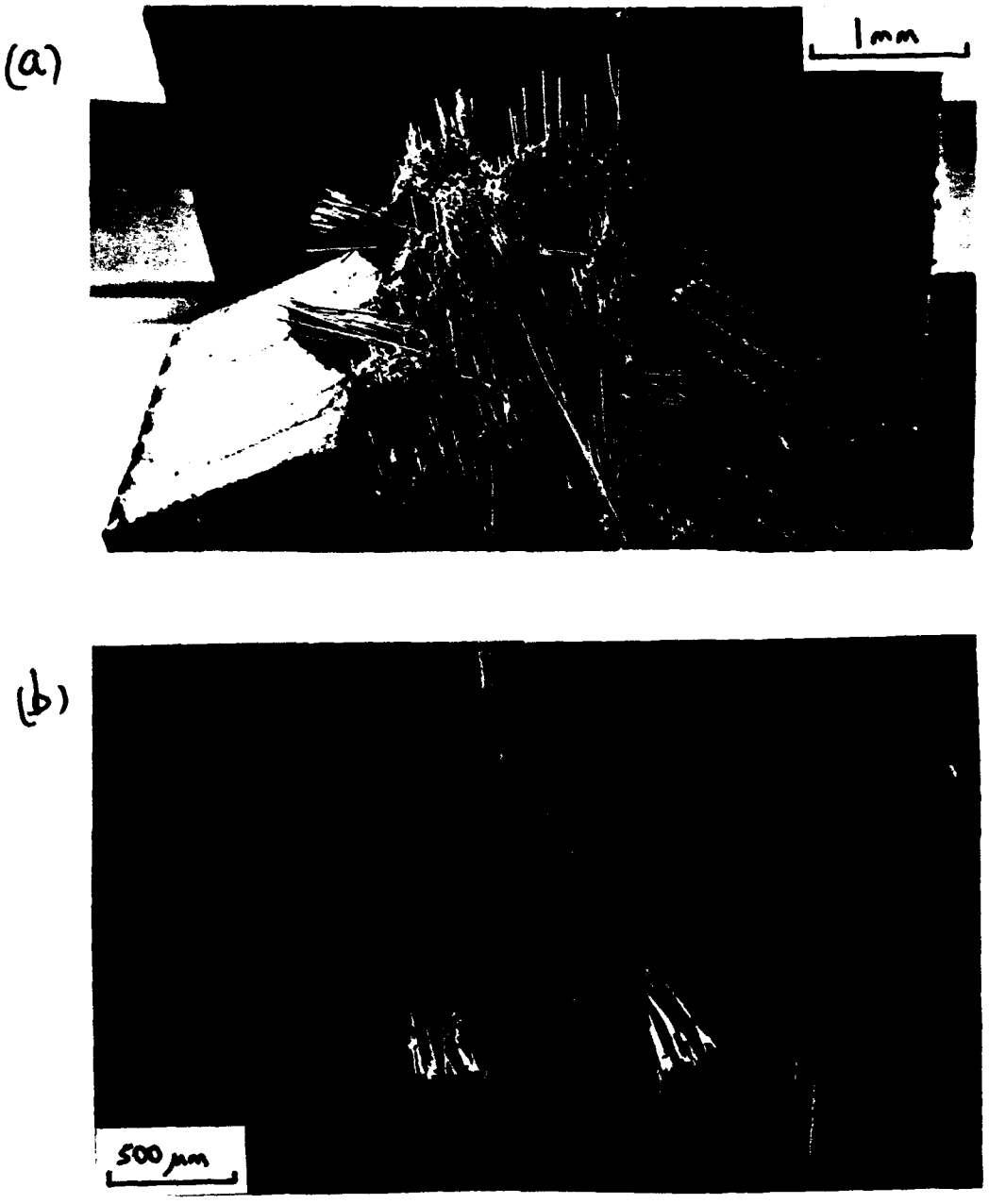

FIG.16 – SEM micrographs of the two fracture surfaces (a,b), showing extensive fibre pullout, and 90 ply failure away from the notch root.

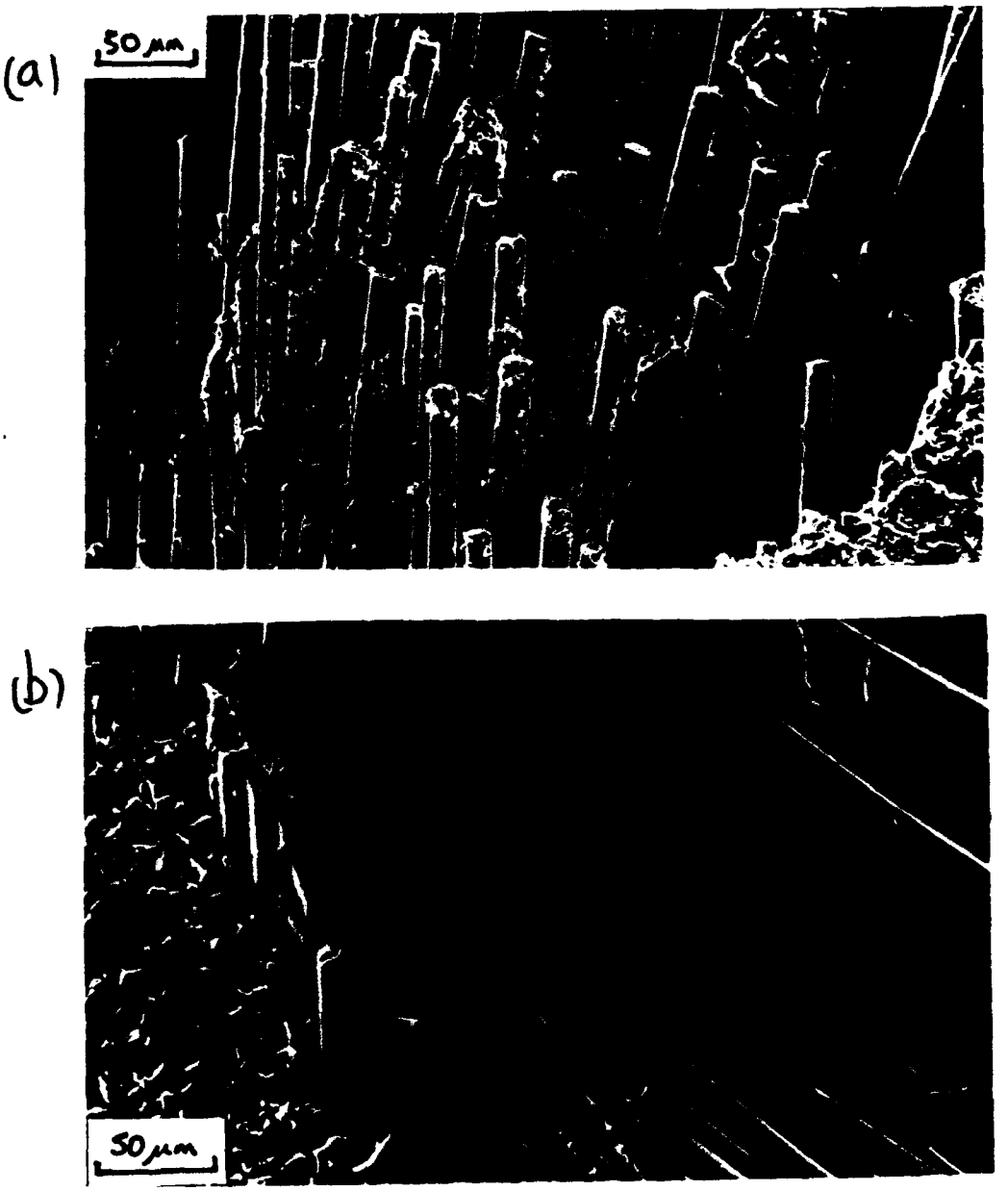

FIG.17 – SEM micrographs showing details of the fracture surface: (a) 0 fibres at a range of lengths, with some glass fragments adhering to the fibres; (b) fibre waviness in the 90 ply which led to low angle bridging of transverse ply cracks.

In the CAS–glass material the statistical variability of fibre and ply strength is more significant, so failure is not so localised in spite of the stress concentration of the notch. The material thus shows very weak notch sensitivity, firstly because the damage reduces the stress concentration, and secondly because the strength variability of the material spreads individual fibre failures over a wider region.

The in–situ test with a V–notch thus indicated some parallels and some differences between the CAS/SiC material and conventional polymeric composites. There were some drawbacks with this test: the loads required were around 2kN, which was approaching the limit of the in–situ rigs; only damage in the notch could be observed, whereas it was desirable to see both the notch and specimen surface simultaneously; the detail of the cracking sequence at the notch root could not be distinguished. Furthermore fatigue loading in–situ could only be realistically achieved over 10 or 20 cycles. Subsequent tests were therefore conducted on conventional screw–driven test machines, but were interrupted for SEM observation of the damage using a rotating stage which allowed all sides of the specimen to be observed. Alternative notch shapes were also used which were easier to prepare, and which gave a clearer view of the damage. This also allowed an evaluation of the influence of notch shape on the failure process.

2.4.2 Effect of notch shape

Rectangular notch

A rectangular notch was cut using a 0.4mm diamond wheel normal to the specimen edge. The root of the notch was flat with a good finish, so the initiation of cracks could be observed. Notch depth was reduced to $2a/w = 0.5$. The damage which formed followed the same pattern as in the V–notched test – Table 3 shows the remote stress applied at various levels of damage.

Table 3: Damage evolution with remote stress in double edge–notched tension test

Damage state	Remote stress	% of failure stress
90^0 ply cracks at notch corners	87 MPa	46%
90^0 ply cracks at notch centre and 0^0 ply matrix cracks	148 MPa	78%
Delaminations and splits at some interfaces	169 MPa	89%
Catastrophic failure	190 MPa	100%

Table 3 shows that the sharp corners of the rectangular notch nucleate transverse cracks at a lower stress than those which formed in the notch centre. Even so the cracking stress was surprisingly high, as the actual stress on the central ligament is in excess of twice the remote value. Multiple matrix cracks formed in the notch root in the 0^0 ply (Fig.18a), some by extension of 90^0 cracks which had appeared at a lower stress (Fig.18b). Zawada *et al.* (1991) also observed that 90^0 ply cracks precede 0^0 cracks in tests on the same cross–ply material with unnotched specimens; Pryce and Smith (1992) have likewise observed 90^0 cracks extending into the adjacent 0^0 plies in a CAS–ceramic/SiC material. 0^0 ply cracks are important as they locally raise the fibre stress and thus influence the statistical failure of fibres.

Prior to failure it was possible to see the splits in the surface 0^0 plies with the naked eye. Subsequent examination of the failed specimen (Fig.19a) clearly showed one surface split extending from the notch root. The smaller notch depth meant that the delaminations reached the specimen edge prior to failure. They then propagated a considerable distance along the edge. For $2a/w = 0.5$ in CFRP the delaminations do not reach the free edge, so there is a greater tendency to delaminate in this material. Note that the anisotropy between 0^0 and 90^0 plies is much smaller in this material, so the delamination is due to much lower interfacial toughness rather than due to high

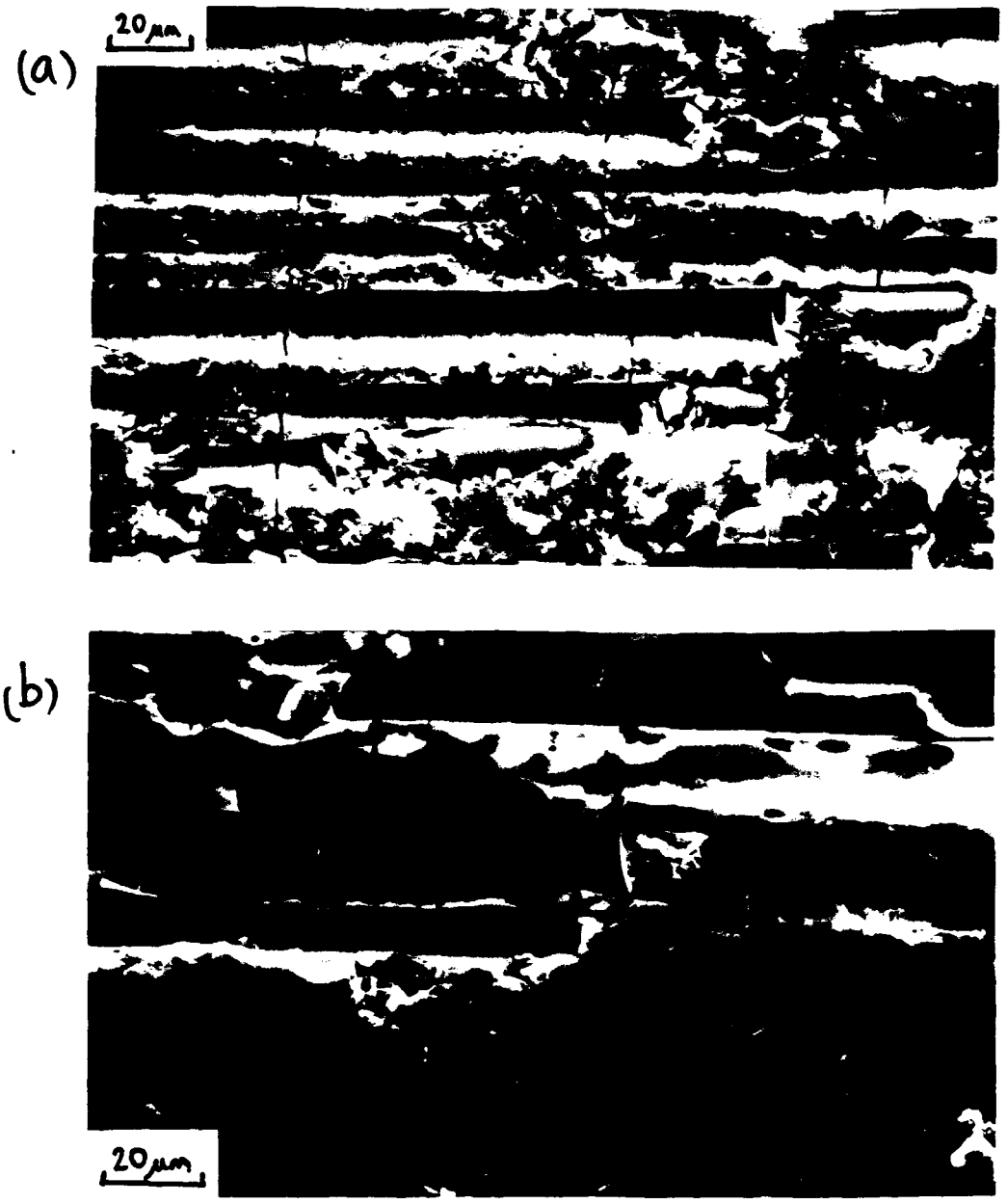

FIG. 18 – SEM micrographs of matrix cracks in the notch root; in (b) the 90 ply crack formed first and later extended into the 0 ply.

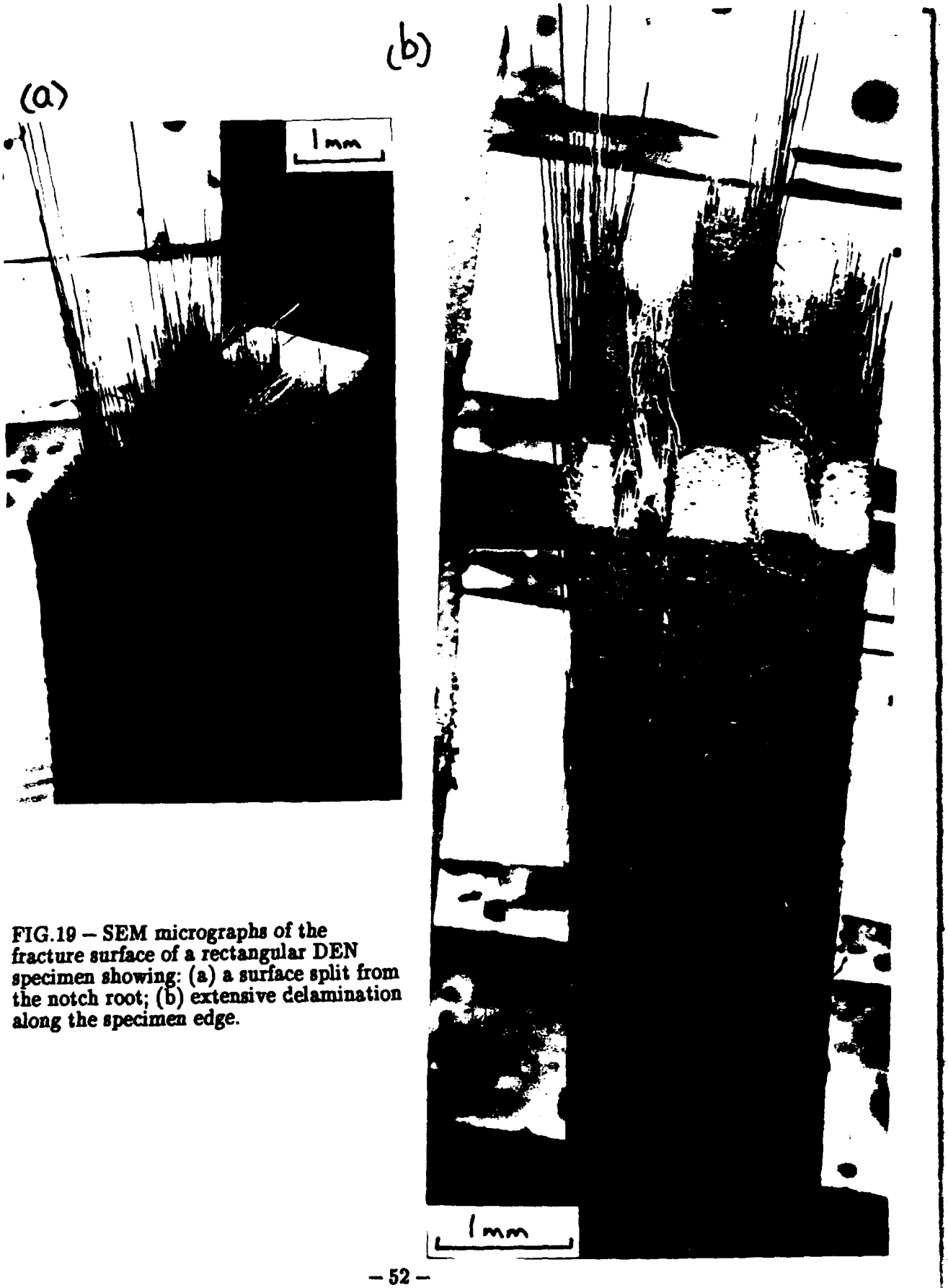

FIG.19 – SEM micrographs of the fracture surface of a rectangular DEN specimen showing: (a) a surface split from the notch root; (b) extensive delamination along the specimen edge.

interfacial shear stresses. Failure was accompanied by further propagation of both splits and delaminations. Figure 19b shows the extent of the delaminations after failure – they have propagated along virtually the whole specimen gauge length. Note also that the remote failure stress in a repeat test with a rectangular notch was 231 MPa (as compared with 190 MPa in the first test), an indication of the possible scatter in data for this material, as is also found with polymeric materials.

Semi–circular notch

Semi–circular edge–notches were produced by drilling several holes with diamond drill bits of diameter 4mm, and then cutting out specimens through the hole centres. It was found difficult to drill through the material without the 0^{o} ply on the back face becoming damaged around the hole. Specimens need to be held firmly against a hard backing material, such as alumina. Tests were continued with damaged specimens provided the extent of damage to the load–bearing fibres was small, though observation of damage growth on the damaged face was somewhat impeded.

The static behaviour of a specimen with a semi–circular edge notch, with $2a/w = 0.5$, was very similar to that with a rectangular notch, described above. Cracking at the notch root could not be observed clearly due to the rough curved finish. Splits formed at around 80% of the failure load, and were again visible to the naked eye. The terminal damage state is shown in Figure 20 – a view showing the specimen surface and edge with half of one notch. Delaminations have extended from the notch root out to the free edge and along the edge, while the split from the notch root in the surface ply consists of a band of damage rather than as a single well–defined crack. The remote stress at failure was 211 MPa, which is exactly halfway between the two values measured for rectangular notched specimens. It would therefore appear that for a given $2a/w$ the notch shape has little effect on the damage and failure stress – the stress concentration at the notch root is blunted by the splits and delaminations, which leads to good notch insensitivity. Notch depth to width ratio is more significant as the

FIG.20 – SEM micrograph of the terminal damage state for a circular DEN specimen; the surface split from the notch root is a band of damage rather than a single crack.

damage pattern can vary with 2a/w if, for example, delaminations reach a free edge. This effect has also been noted for CFRP – the model for self–similarity of damage remained valid only so long as the delaminations remained within the bulk of the material.

2.4.3 Fatigue tests – observations of damage and failure

Fatigue loading of CFRP causes the static damage to propagate, at a rate which falls steadily as the split length increases. Typically maximum stresses of the order of 70% of the static failure stress are required in fatigue (for an R–ratio near zero) to cause measurable damage growth in under 10^6 cycles. Fatigue tests were therefore made on the CAS–glass/SiC material at peak stresses above 70% of the static strength, in the expectation that damage growth would occur in a relatively small number of cycles. Fatigue loading was achieved on a screw–driven machine in its cyclic mode, at a frequency of approximately 0.2 Hz. The R–ratio, P_{min}/P_{max} was maintained at 0.1 throughout.

Semi–circular notch

A specimen with a semi–circular notch, 2a/w = 0.5, was fatigued at $\Delta\sigma = 160$ MPa (for which σ_{max} was roughly 82% of the static failure value). The first cycle was thus sufficient to initiate TPCs, splits and delaminations, close to the damage state shown in Fig.20. After 150 cycles the damage had propagated, as illustrated in Fig.21. Figure 21a shows one face of the specimen – splits have grown from the notch roots in all four directions possible, but as bands of damage which have broadened towards the specimen centre near the lower notch. Viewed from the side (Fig.21b) it is apparent that the 0^o surface plies have sustained some damage, with many broken fibres protruding from the surface. Delaminations have also run along all the 0/90 interfaces down the specimen edge. Figure 21c shows that the delaminations are of two types –

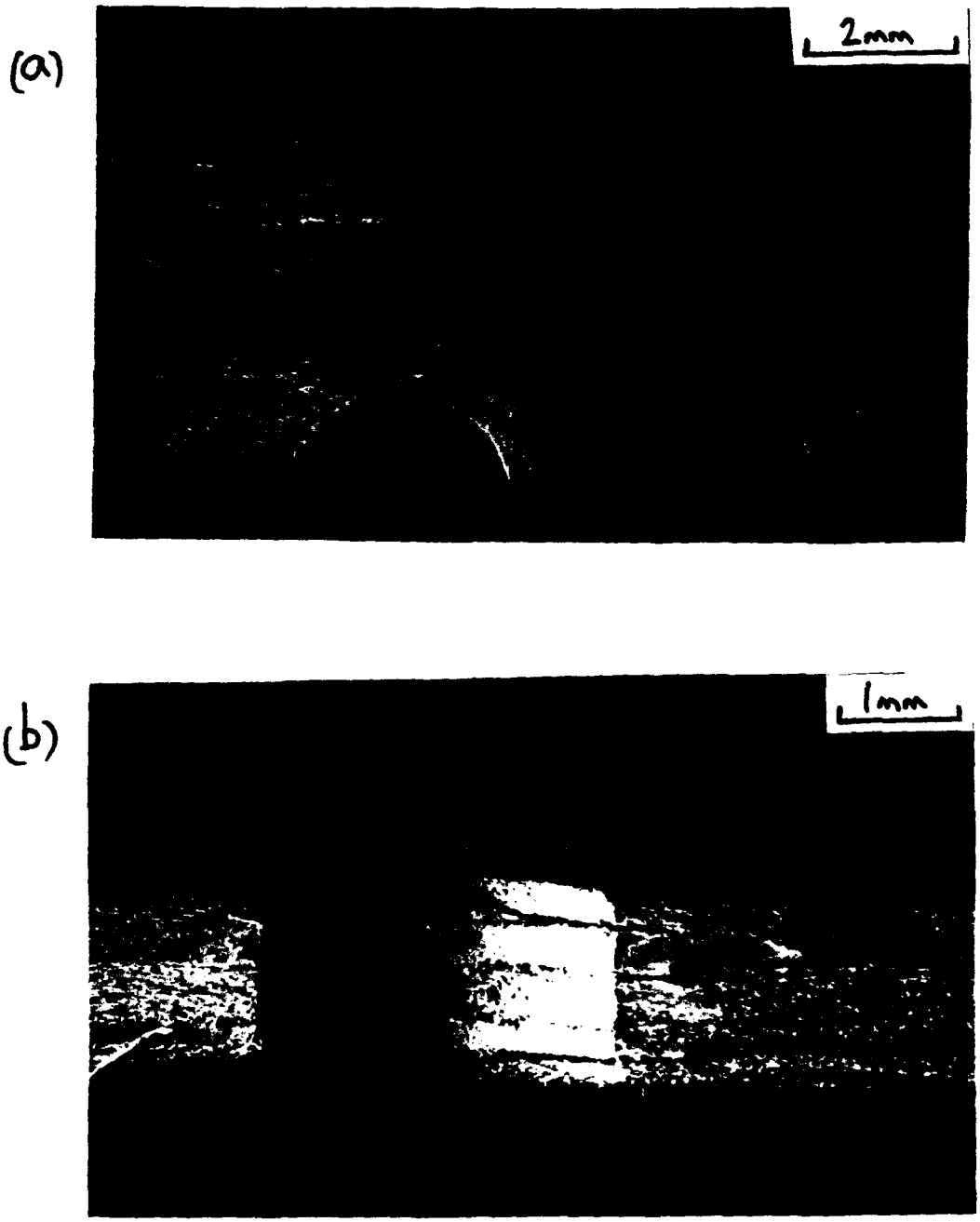

FIG.21 – SEM micrographs of damage growth in fatigue loading of a circular DEN specimen, $\Delta\sigma = 160$ MPa, $R = 0.1$: (a) surface of specimen, after 150 cycles; (b) edge of view of notch region, after 150 cycles.

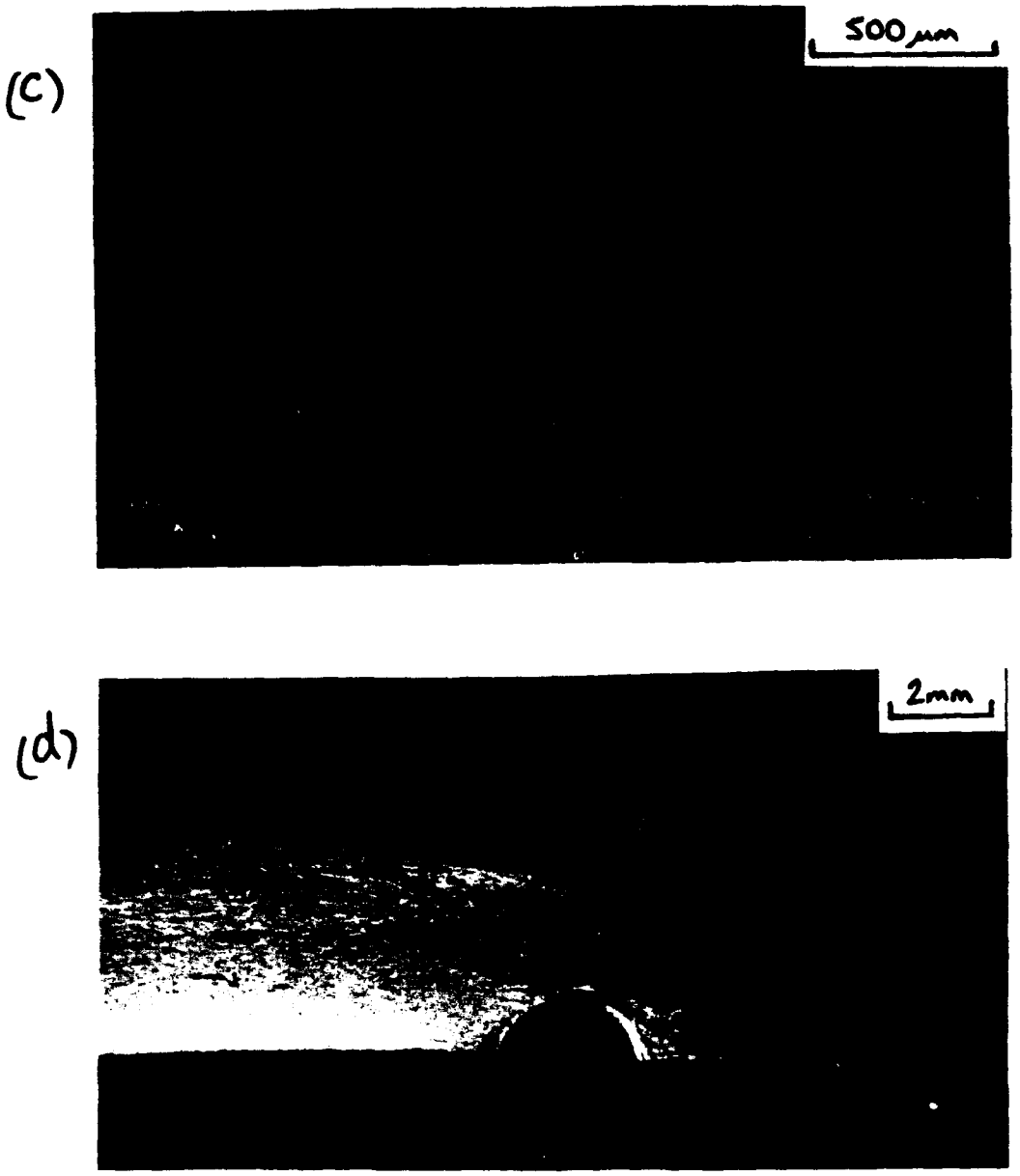

FIG.21 (Continued)
(c) two types of delamination crack along specimen edge.
(d) surface (as in Fig.21a) after 400 cycles.

either one or two fibres inside the 90^{O} ply (and linking up in the lower 90^{O} ply), or one or two fibres inside the 0^{O} ply. The number of cycles was increased to 400, causing further damage propagation. Figure 21d shows the same face as in Fig.21a at N = 400 – the 0^{O} ply damage is more marked with additional splits having formed away from the notch root.

The specimen was then pulled to failure, which caused further damage – Fig.22a shows the same face of the specimen after failure: fibres have parted in a broad band between the notches, but the damage is extensive away from the notches too. On the opposite face however, the 0^{O} ply failure is 5mm to one side of the notch, linking the two splits at a point of lower stress concentration (Fig.22b). Viewed edge–on the delamination damage is apparent (Fig.22c). Very long delaminations have formed, and the specimen has come apart more severely than in the static tests. As fibre failures have occurred over a considerable length, the specimen remained intact after failure due to the long pullout lengths, in spite of the severe damage particularly around the notch (Fig.22d).

It is therefore clear that in common with CFRP and other polymeric systems, fatigue loading causes damage propagation, which would in principle diminish the stress concentration at the notch and increase the failure strength. It is apparent in this material however that the properties of the 0^{O} ply in particular are degraded by fatigue, with premature fibre failures occurring, so the strength would on this account be reduced. The residual strength after 400 cycles was 229 MPa, which is slightly higher than in the static test with this shape of notch, but essentially unchanged within the scatter of the data. Hence for the conditions chosen here the two effects have cancelled out. It is anticipated that further fatigue loading would be detrimental, as fibre failures will progressively raise the stress on the fibres remaining intact. However it is also clear that the material can withstand considerable fatigue damage without loss of strength, though it is likely that there will have been some loss of stiffness. Similar behaviour has been found in fatigue with unnotched specimens of this material by Zawada *et al.* (1991).

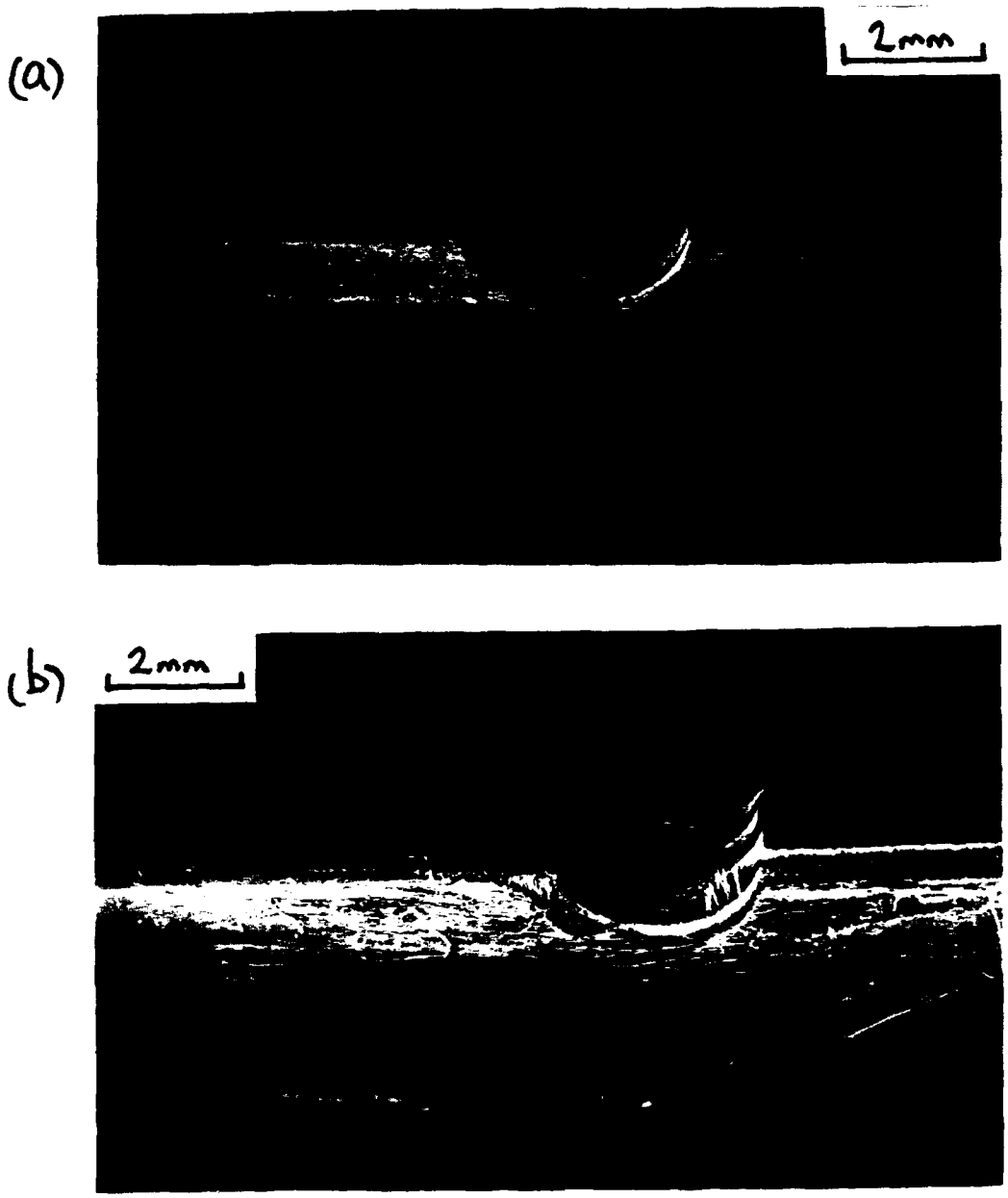

FIG.22 – SEM micrographs of the circular DEN specimen, pulled to failure after 400 cycles: (a) surface failure, on the side shown in Figs.21a,d; (b) surface failure, well away from the notch, on the opposite face.

FIG.22 (Continued)
(c) edge view of extensive delaminations.
(d) view of the notch region, showing 0 fibre failures and opening of the delaminations.

Rectangular notch

A slightly lower stress level was used in this test, and applied for a greater number of cycles. $\Delta\sigma$ was 153 MPa, giving a peak stress around 75% of the static failure stress. The test was interrupted after one cycle, at which time the damage had just nucleated: fine splits from the notch root (Fig.23a) and delaminations just extending along the specimen edge from the lip of the notch (Fig.23b). Further SEM observations were made after 30, 150 and 800 cycles. An attempt was made to measure split length eact time the test was stopped. On the whole the split tips could be located with reasonable certainty, as the faces had been partially polished prior to testing. However there was too much scatter in the data with splits nucleating after widely different numbers of cycles so that the final split lengths at N = 800 varied between 0.8mm and 6.1mm. It was also found that delaminations only grew on some 0/90 interfaces – Figure 24a shows that at N = 800 there were 4 delaminations to one side of one of the notches, but only one on the other. It was noted however that extensive splits coincided with long delaminations along the edge of the same 0^{o} ply, so the two types of crack are linked in this material too. There was relatively little damage in the root of the notch after 800 cycles – Fig.24b shows very few matrix cracks, without the extensive 0^{o} fibre damage observed at the higher loads of the previous test. A tilted view of the central 0^{o} ply in the notch root showed that some fibres were bowed (Fig.24c), indicating that some irreversible debonding and sliding has taken place. In time this behaviour would lead to isolated fibre failures and ply degradation.

The specimen was again pulled to failure, breaking at a stress of 203 MPa. Again the failure stress is not significantly different to the static value. In this test all of the 0^{o} plies failed at locations away from the notch. Figure 25a shows a surface ply failure 4mm away from the notch. Note also the long splits and associated delamination of the first 0/90 interface. The post–fatigue failed specimen was again more severely damaged than after a static test (compare Fig.25a with Fig.19b). As the pullout lengths were increased by fatigue, the two halves of the specimens were more firmly held together

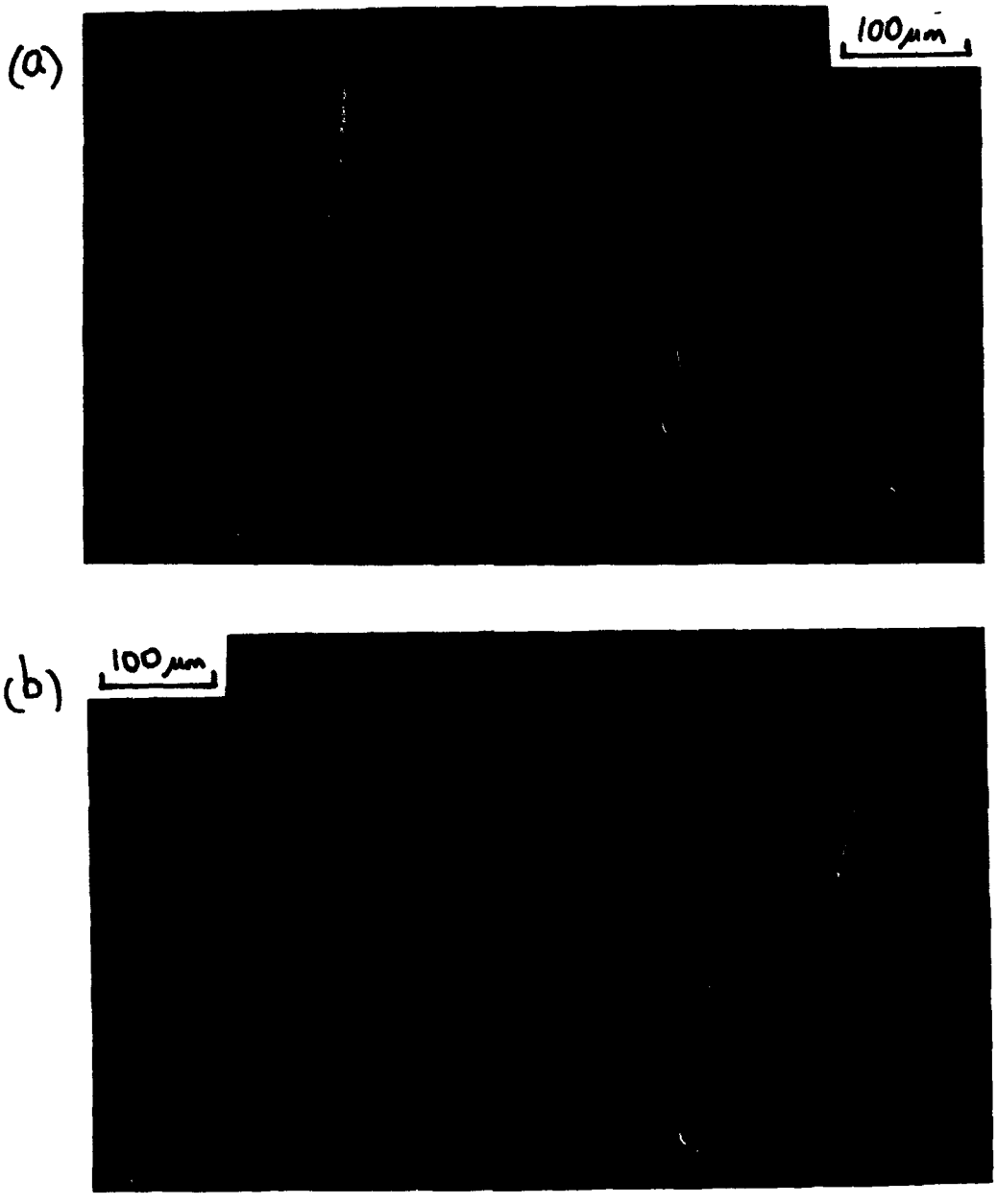

FIG.23 – SEM micrographs of the damage after one cycle at $\Delta\sigma = 153$ MPa, R = 0.1, for a rectangular DEN specimen: (a) split from notch root; (b) onset of delamination on edge of specimen.

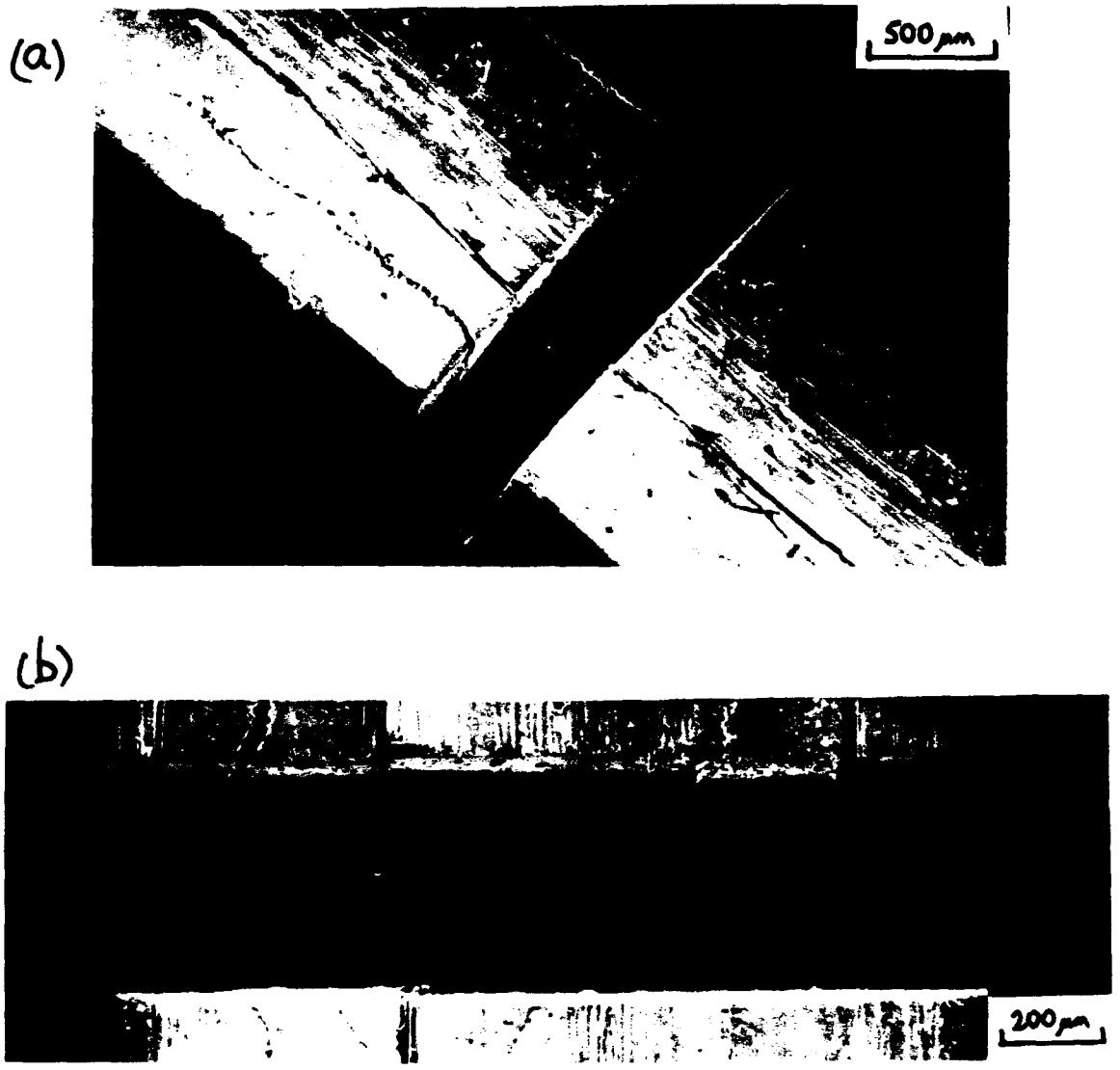

FIG.24 – SEM micrographs of the damage after 800 cycles at $\Delta\sigma = 153$ MPa, R = 0.1, for a rectangular DEN specimen: (a) asymmetry of delaminations; (b) minimal damage at the notch root.

(c)

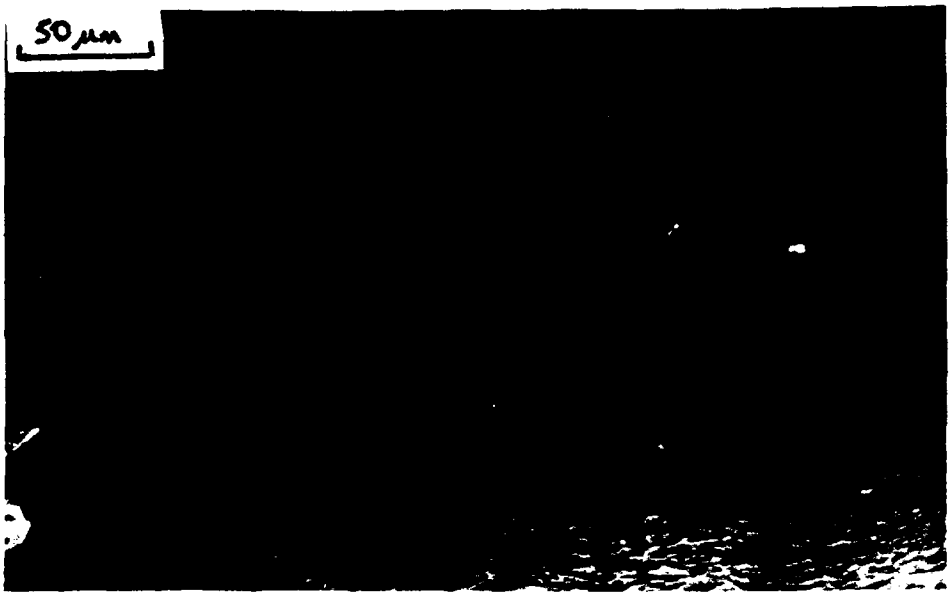

FIG.24 (Continued)
(c) bowed 0 fibres indicating that some irreversible sliding and damage has occurred.

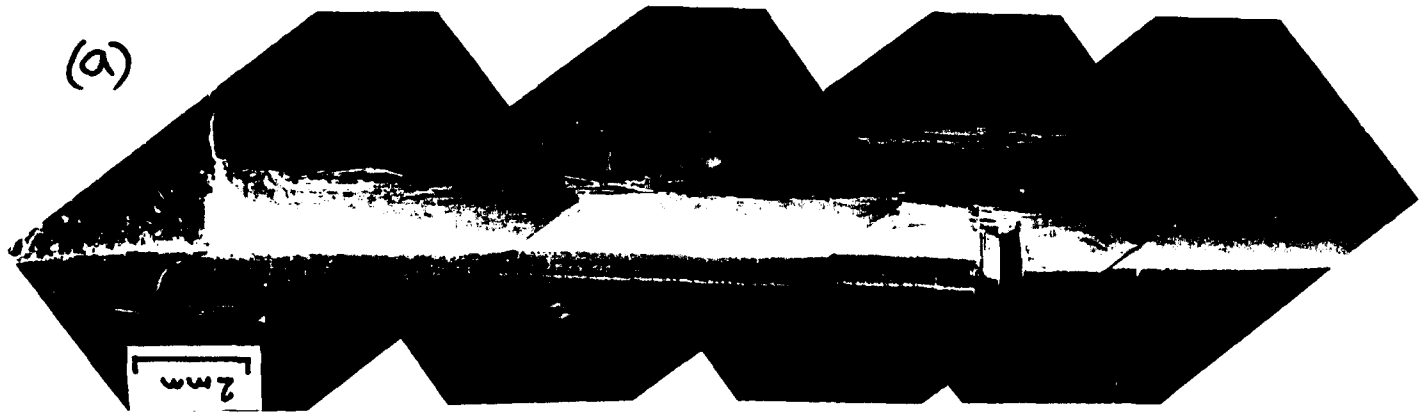

FIG.25 – SEM micrographs of the rectangular DEN specimen, pulled to failure after 800 cycles at $\Delta\sigma = 153$ MPa, R = 0.1: (a) 0 ply failure away from the notch, and extensive splits and delaminations.

(b)

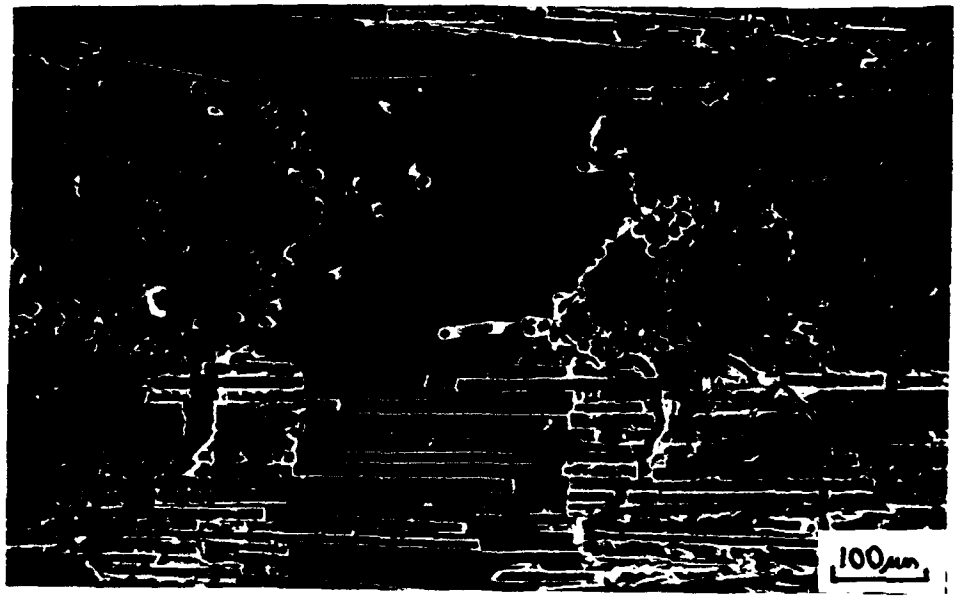

(c)

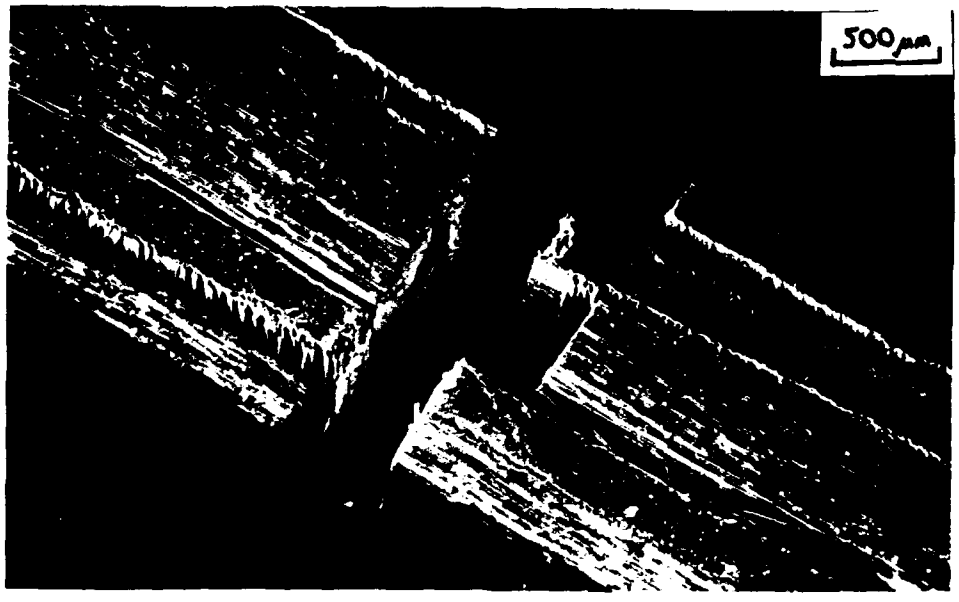

FIG.25 (Continued)
(b) transverse ply crack associated with 0 ply failure, showing pullout of 0 fibres.
(c) view of notch region showing relative sliding of some 0 plies.

FIG.25 (Continued)
(d) two types of delamination – just inside either a 0 or a 90 ply.

after failure. The location of a 0^{O} ply failure was often associated with a 90^{O} crack opening up (Fig.25b), suggesting that the critical 0^{O} matrix crack formed initially in the 90^{O} ply alongside and propagated across the interface. Figure 25b also shows the extensive fibre pullout occurring when a 0^{O} ply failed. As neighbouring plies failed at different locations, mostly away from the notch, the failure caused adjacent plies to slide past one another, leaving a jogged edge to the original notch (Fig.25c). Two types of delamination were again observed, slightly within either a 0^{O} ply or a 90^{O} ply (Fig.25d).

2.3.5 Summary and conclusions

The test series on double edge–notched tension specimens has indicated that the behaviour established for polymeric systems is followed up to a point, but significant deviations then occur. In summary, first for static loading:

(i) sub–critical damage develops in the form of transverse ply cracks, delaminations and splits;

(ii) the TPCs are less dense, and away from the notch form by deviation of delamination cracks away from the 90/0 interface;

(iii) the tendency to delaminate is more marked than in CFRP;

(iv) there is more statistical variation in the damage which forms, but failure occurs when the damage has reached a characteristic state, i.e. when load redistribution due to the damage causes the strength of the 0^{O} plies to be exceeded;

(v) 0^{O} ply failure occurs by single fibre and bundle failure at locations distributed in the material, not around the root of the notch, leading to extensive fibre pullout and energy dissipation at failure.

(vi) the material is very notch insensitive, and at a given notch depth the failure stress is essentially independent of notch shape;

(vii) changes in notch depth can lead to marked differences in behaviour if the delaminations reach the specimen edge, where they can propagate much more easily;

Fatigue loading has then shown the following:

(i) the damage propagates, in principle reducing the notch stress concentration further;

(ii) fatigue loading degrades the 0^{o} ply properties causing irreversible slip of fibres and fibre failure, notably above about 80% of the static failure stress; this counteracts the effect of (i) and will eventually lead to failure in itself.

(iii) the damage propagation in fatigue is irregular with some splits and delaminations growing extensively while others do not at all;

In conclusion, this material is more problematic in terms of applying damage mechanics and the modelling used for CFRP. The damage is not consistent enough and the ply properties are more statistically variable, so the location of failure is much less determinate. The results are encouraging however from the point of view of notch insensitivity, and the retention of strength under moderate fatigue loading.

3. CONCLUSIONS

(a) In all the geometries considered, sub–critical damage develops prior to final failure. In four–point bend and edge–notched tension in particular the damage state immediately prior to final failure has a strong influence on the strength, in common with conventional polymeric long–fibre composites. This also determines the overall work of fracture. The damage is generally complex, making modelling of fracture behaviour difficult, but the work has highlighted the need for an accurate picture of the sub–critical damage before modelling work is undertaken. This has often not been the case in the literature.

(b) The in–situ SEM facility is a powerful tool for accurately observing the growth of damage and the interaction of different cracks. The observations illustrated here are beyond the capabilities of most optical techniques. Dynamic observation is particularly useful in these materials, since at failure the damage propagates, rendering post–mortem examination misleading.

(c) The four–point bend test with a through–ply surface notch is perhaps over–rated as a test of the strength of these materials. The damage which forms is variable, depending on notch depth and local fibre waviness; the failure mechanism changes with variations in damage and specimen dimensions; tensile failure, if it occurs, is subject to wide variations due to the statistical fluctuations in 0^{O} ply properties. Elaborate modelling of bridged delaminations in this geometry does not appear justified.

(d) more reproducible delamination behaviour is observed in double cantilever beam specimens. A marked R–curve develops, albeit over unrealistic crack lengths and openings. The observations indicate that tensile stresses in bridging fibres are important, contrary to previous thinking, and this combined with the knowledge of the geometric disposal of bridging fibres across the crack provides insight into the resistance to the more practically important mode II delamination behaviour.

(e) the notched tensile behaviour of these materials is complex, but in some respects mirrors the behaviour seen in polymeric materials. The major deviations are in

the low density of transverse ply cracks, and the ease of delamination. Modelling of the stresses in the damaged condition would be difficult, due to the lack of self–similarity in damage observed. The material is however notch insensitive, and can withstand many cycles of fatigue loading at stresses up to approximately 80% of the static strength without any loss of residual strength.

REFERENCES

Aveston J., Cooper G.A. and Kelly A. (1971), Proc. NPL Conf. on Properties of Fibre Composites, pp.15–26.

Bao G., Fan B. and Evans A.G. (1991), Univ. of California at Santa Barbara, University Research Initiative Report, January 1991.

Bao G., Ho S., Fan B. and Suo Z. (1991), Univ. of California at Santa Barbara, University Research Initiative Report, January 1991.

Bao G., Ho S., Fan B. and Suo Z. (1992), Univ. of California at Santa Barbara, University Research Initiative Report, January 1992.

Beyerle D.S., Spearing S.M., Zok F.W. and Evans A.G. (1992), Univ. of California at Santa Barbara, University Research Initiative Report, January 1992.

Bordia R.K., Dalgleish B.J., Charalambides P.G. and Evans A.G. (1991), J.Am.Ceram.Soc. 74(11), pp.2776–2780.

Budiansky B., Hutchinson J.W. and Evans A.G. (1986), J.Mech.Phys.Solids 34, pp.164–189.

Cao H.C., Bischoff E., Sbaizero O., Ruhle M. and Evans A.G. (1990), J.Am.Ceram.Soc. 73(6), pp.1691–1699.

Cox B.N. (1991), Acta metall. mater. 39(6), pp.1189–1201.

Cox B.N. and Lo C.S. (1992a), Acta metall. mater. 40(1), pp.69–80.

Cox B.N. and Lo C.S. (1992b), Acta metall. mater., in press.

Cox B.N. and Marshall D.B. (1991), Acta metall. mater. 39(4), pp.579–589.

Curtin W.A. (1991), J.Am.Ceram.Soc. 74(11), pp.2837–2845.

Dimant R.A., Shercliff H.R. and Beaumont P.W.R. (1992), Cambridge University Engineering Department Technical Report, in preparation.

Evans A.G. (1990), J.Am.Ceram.Soc. 73(2), pp.187–206.

Evans A.G. and Marshall D.B. (1989), Acta metall. 37(10), pp.2567–2583.

Handbook of Materials Science (1974), Vol.2 (Ed. Lynch C.T.), CRC Press.

Harris B., Cooke R.G. and Habib F.A. (1992), Proc.ECCM5, Bordeaux, April 1992, pp.605–611.

Harris B., Habib F.A. and Cooke R.G. (1992), Proc.R.Soc.Lond. A437, pp.109–131.

Hashemi S., Kinloch A.J. and Williams G. (1991), in Composite Materials: Fatigue and Fracture (Third Vol.), ASTM STP1110 (Ed. O'Brien K.), ASTM, Philadelphia, pp.143–168.

He M.Y., Cao H.C. and Evans A.G. (1990), Acta metall. mater. 38(5), pp.839–846.

He M.Y. and Evans A.G. (1992), submitted to J.Comp.Tech. and Research.

Heredia F.E., Spearing S.M., Evans A.G., Mosher P. and Curtin W.A. (1992), Univ. of California at Santa Barbara, University Research Initiative Report, January 1992.

Kaute D., Shercliff H.R. and Ashby M.F. (1992), in preparation.

Kortschot M.T. and Beaumont P.W.R. (1990a,b), Composite Science and Technology 39, pp.289–301 and 303–326.

Kortschot M.T., Ashby M.F. and Beaumont P.W.R. (1991a,b), Composite Science and Technology 40, pp.147–165 and 167–179.

Larsen D.C. and Stuchly S.L. (1990), Ch.7 in "Fibre Reinforced Ceramic Composites – Materials, Processing and Properties", Noyes Publications, New Jersey.

Marshall D.B., Cox B.N. and Evans A.G. (1985), Acta metall. 33(11), pp.2013–2021.

Marshall D.B. and Cox B.N. (1987), Acta metall. 35(11), pp.2607–2619.

Marshall D.B. and Evans A.G. (1985), J.Am.Ceram.Soc. 68(5), pp.225–231.

Prewo K.M. (1986), J.Mats.Sci. 21, pp.3590–3600.

Prewo K.M. (1989), Ceramic Bulletin 68(2), pp.395–400.

Pryce A.W. and Smith P.A. (1992), J.Mats.Sci.27, pp.2695–2704.

Pysher D.J., Goretta K.C., Hodder R.S. and Tressler R.E. (1989), J.Am.Ceram.Soc. 72, pp.284–289.

Quinn G.D. and Morrell R. (1991), J.Am.Ceram.Soc. 74(9), pp.2037–2065.

Rouby D. and Navarre G. (1990), Proc. 11th Riso Int.Symp. on Metallurgy and Materials Science, Sept.1990, pp.127–144.

Sbaizero O., Charalambides P.G. and Evans A.G. (1990), J.Am.Ceram.Soc. 73(7), pp.1936–1940.

Shercliff H.R., Vekinis G., Ashby M.F. and Beaumont P.W.R. (1992), Cambridge University Engineering Department Technical Report, CUED/C–MATS/TR198, March 1992.

Sorenson B.F., Talreja R. and Sorenson O.T. (1992), Proc.ECCM5, Bordeaux, April 1992, pp.613–618.

Spearing S.M. and Beaumont P.W.R. (1992a,b), Composite Science and Technology 44, pp.159–168 and 299–307.

Spearing S.M., Beaumont P.W.R. and Ashby M.F. (1992c), Composite Science and Technology 44, pp.169–177.

Spearing S.M., Beaumont P.W.R. and Smith P.A. (1992d), Composite Science and Technology 44, pp.309–317.

Spearing S.M., Beaumont P.W.R. and Kortschot M.T. (1992e), Composites 23(5), pp.305–311.

Spearing S.M. and Evans A.G. (1992), Acta metall. mater. 40(9), pp.2191–2199.

Suo Z. (1990), J.Appl.Mech. 57, pp.627–634.

Suo Z., Bao G. and Fan B. (1992), J.Mech.Phys.Solids 40(1), pp.1–16.

Suo Z., Bao G., Fan B. and Wang T.C. (1991), Univ. of California at Santa Barbara, University Research Initiative Report, January 1991.

Thouless M.D. and Evans A.G. (1988), Acta metall. 36(3), pp.517–522.

Thouless M.D., Sbaizero O., Sigl L.S. and Evans A.G. (1989), J.Am.Ceram.Soc. 72(4), pp.525–532.

Weihs T.P., Sbaizero O., Luh E.Y. and Nix W.D. (1991), J.Am.Ceram.Soc. 74(3), pp.535–540.

Zawada L.P., Butkus L.M. and Hartmann G.A. (1991), J.Am.Ceram.Soc. 74(11), pp.2851–2858.

Zok F.W., Sbaizero O., Hom C.L. and Evans A.G. (1990), J.Am.Ceram.Soc. 74(1), pp.187–193.

Zok F.W. and Spearing S.M. (1992), Univ. of California at Santa Barbara, University Research Initiative Report, January 1992.

B. PROCESSING OF TOUGHENED ALUMINA

1. INTRODUCTION

It is now well known that the incorporation of a dispersed ductile phase in a brittle ceramic material can lead to very significant enhancement of flaw tolerance and fracture toughness (up to a factor of 15 in WC–Co). However, only the well–documented WC–Co system (e.g.Lueth, 1974; Sigl and Exner, 1987; Sigl *et al.*, 1988) has been fully developed and is technologically successful. It is used very widely for its wear resistance as tooling but has various limitations, notably its high density and low corrosion resistance. In the past few years a number of reports have appeared on efforts to develop and characterise the Alumina–Al system, produced by various routes – a controlled oxidation, or LANXIDE^{R}, process (Newkirk *et al.*, 1986, 1987; Sigl *et al.*, 1988; Aghajanian *et al.*, 1989; Flinn *et al.*, 1989); and the liquid pressure forming process (Mykura, 1992). Other material systems include alumina with iron or nickel particles (Sun *et al.*, 1991) as well as toughened intermetallics, such as TiAl with Nb or TiNb (Cao *et al.*, 1989; Deve *et al.*, 1990; Venkateswara Rao *et al.*, 1992), TiTaAl with W (Deve and Maloney, 1991) and $MoSi_2$ with Nb (Lu *et al.*, 1991; Besson *et al.*, 1992). Various glass–metal systems (e.g.Krstic *et al.*, 1981; Ashby/Bannister *et al.*, 1989, 1991, 1992; Shaw *et al.*, 1990) have been reported mainly for modelling purposes. Most of these systems consist of interconnecting networks of the two phases; the primary mechanisms responsible for their toughening are bridging by intact ligaments of the ductile phase in the wake of the advancing crack tip (Evans and McMeeking, 1986) and plastic straining of ductile particles in the process zone which results in crack shielding (Sigl *et al.*, 1988) These micromechanisms result in pronounced R–curve behaviour (increase in toughness with crack growth) whose shape (extent and steepness) determines the mechanical properties of a specimen made from the material.

Reinforcement of ceramic matrices by ductile inclusions has a number of potential applications. Optimally it results in isotropic materials with elastic properties close to the properties of the ceramic but with enhanced energy dissipation characteristics. The use of refractory inclusions can enable high temperature applications and if care is taken to ensure that all inclusions are enclosed by the matrix then corrosive environments would not present a problem. Under certain conditions such materials are well suited to applications where a large number of cracks are generated simultaneously such as in high impact armouring.

The development of metal–reinforced ceramics has been greatly enhanced by theoretical and experimental modelling (Sigl and Exner, 1987; Sigl *et al.*, 1988; Evans and McMeeking, 1986) and notably by the work carried out by Ashby, Bannister and co–workers (1989, 1991, 1992). This modelling work has been instrumental in determining the important toughness–controlling parameters such as the decohesion length and associated interfacial strength. That work has paved the way towards designing new composites having optimum energy–dissipation characterisitics.

Briefly, toughening in metal–reinforced ceramic systems takes place as follows (Fig.1a): a propagating crack in a brittle matrix is intercepted by ductile inclusions. Energy is dissipated by the work done in deforming the inclusions in the bridging zone until failure and, to a lesser extent, by straining the inclusions in the process zone. Model glass–lead experiments have shown that the maximum energy absorbed by deforming the inclusions in the bridging zone at steady state is given by (Ashby *et al.*, 1989):

$$\Delta G_c = V_f \int \sigma(u) = C\, V_f\, \sigma_0\, a_0 \qquad (1)$$

where ΔG_c is the additional energy dissipated per unit area (work of rupture), V_f is the area fraction of the ductile phase intercepted by the crack plane, σ_0 the initial flow stress and a_0 the radius of the particle.

The constant C depends strongly on the interfacial strength between the matrix

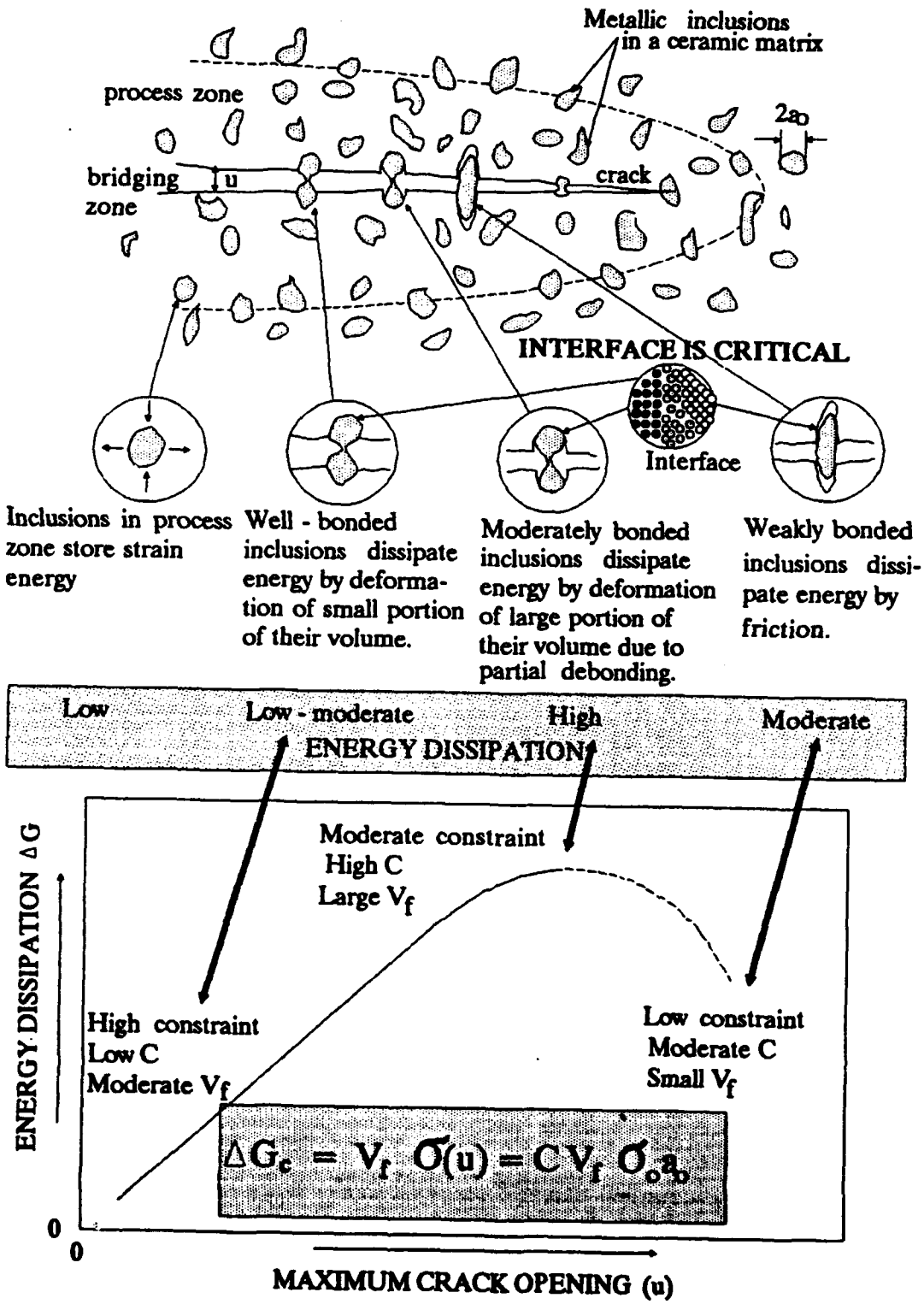

FIG.1 – Schematic representation of toughening of ceramics by ductile inclusions and b) influence of bonding strength on energy dissipation.

and the reinforcing phase and describes the extent of debonding (which affects the failure mechanism). It varies from 1.6 for very strong bonding to about 6 for limited debonding or concentric matrix fracture. Complete debonding (very weak interfacial strength) results in a very low value for C. So strong bonding results in lower energy dissipation than bonding of intermediate strength (Fig.1b). It has been found that a different degree of bonding results in a different energy dissipation mechanism for the same size particle: internal void growth in the case of strong bonding, through decohesion and constrained necking in the case of moderate bonding to frictional sliding in the case of weakly bonded inclusions. The above result can be rewritten as:

$$\Delta K_c = \left[E^2 \, C \, V_f \, \frac{\sigma_o}{E} \, a_o \right]^{1/2} \qquad (2)$$

where ΔK_c is the additional fracture toughness (critical stress intensity) and E the Young's modulus of the reinforcing material, provided $\Delta G_c >> G_o$, i.e. $\Delta K_c >> K_o$.

It can be seen therefore that maximum energy dissipation and maximum toughening can be obtained from inclusions with a high specific strength σ_o/E and a large diameter a_o. So, in "designing" such a composite careful consideration should be given to the properties of the inclusions and the interfacial strength.

The way that toughening builds up with crack extension (R–curve) is also dependent on the debonding extent and on the particle size. The results obtained are shown in Fig.2: increasing particle size produces a steeper R–curve but increasing debonding produces a shallower R–curve.

The modelling work has also investigated the effect of shear failure in the case of non–planar cracks in a model "sandwich" specimen (Bannister and Ashby, 1991). It was shown that in this case too, energy dissipation increases with debond length and with "shear angle", the second being a result of work hardening.

However, it soon becomes apparent (Bannister *et al.*, 1992) that it is only possible to obtain the maximum theoretical energy dissipation from such systems with very long initial cracks, i.e. in real loading situations the material would fail before

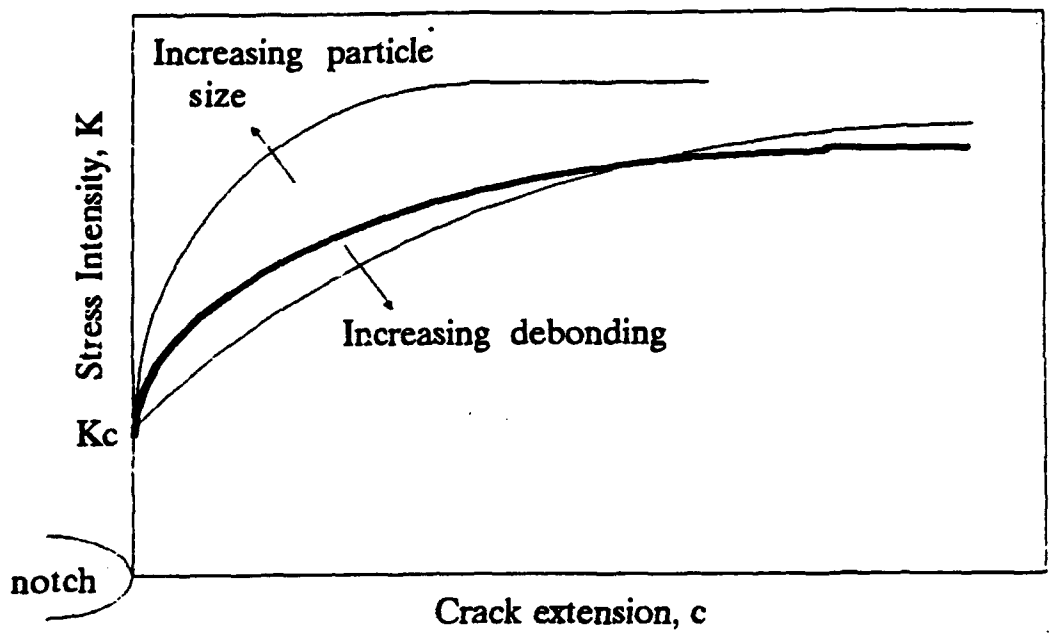

FIG.2 – Effect of increasing particle size and debonding extent on shape of the R–curve.

maximum toughening is obtained. This significant result can be understood as follows. Two conditions must be satisfied in order for a crack to propagate unstably and cause catastrophic failure of a component (K_a being the applied stress intensity):

$$K_a = K_c \tag{3a}$$

$$\frac{dK_a}{dc} = \frac{dK_c}{dc} \tag{3b}$$

So both the magnitude and the rate of change of K are important in determining the stability of crack growth in a material. In most situations the maximum toughness, as given by the steady–state toughness K_{ss}, is not achieved as the conditions in equations (3a,b) are met before the bridging zone is fully developed. From these considerations it is possible to develop "design charts" for metal–reinforced ceramics (Bannister *et al.*, 1992). Materials can then in principle be designed with well–defined energy absorption properties and fracture strength for specific applications. It has also been shown that a rising R–curve in such materials with a dispersion of ductile particles can lead to a transition between single–crack fracture mechanics to multiple–crack damage mechanics. This is shown to result in potentially higher energy absorption at the cost of lower strength.

It should be noted in passing that the R–curve is not a material property, but is very specimen–dependent. Extensive computations of the mechanics of bridged cracks (Cox, 1991; Cox and Lo, 1992a,b; Cox and Marshall, 1991) have indicated that the fundamental property of the composite is the force–opening curve of the bridging ligaments – the "p(u) curve". The R–curve in a given situation is then determined from this curve. The p(u) curve depends directly on the detail of the bridging mechanisms discussed above (constraint of the particles, interfacial debonding, work hardening etc). It is however usually impossible to measure the bridging tractions directly, so it is convenient (if potentially misleading) to discuss the effects in terms of the R–curve, which is easily measurable. During the development of a new material, using one or two simple geometries, the R–curve may be used directly for comparative purposes. Future

application of the material must however take due account of the specimen dependencies highlighted by Cox and co–workers, and attempt to define the bridging behaviour in terms of a p(u) curve.

To summarise, in order to achieve significant amounts of toughening before failure under normal loading conditions, it is necessary to keep the bridging length short while ensuring a high level of steady–state toughness, K_c. Equivalently, the load–displacement "p(u)" curve should peak as quickly as possible and the inclusions should not fail suddenly as strain increases. From the modelling results it would appear that this could be achieved by keeping the size of the particles large while ensuring that they are moderately well bonded to the matrix to give limited decohesion. The actual fracture toughness reached could then be maximised by choosing inclusions with high specific yield strengths σ_0/E (possibly alloys) which work–harden appreciably and by developing processing routes which would allow maximisation of V_f and particle size a_0. Interface control is imperative and may be achieved by coating the ductile inclusions or incorporating boundary phases during processing and controlling specific interphase reactions.

2. EXPERIMENTAL WORK, RESULTS AND DISCUSSION

2.1 Processing Development

One of the basic considerations that has formed a focus during the course of this work has been the premise that utilisation of such materials would be greatly aided if they could be processed using conventional techniques such as uniaxial compaction and pressureless sintering. The intricate and relatively complicated processing routes utilised in the production of such materials till now have been a serious obstacle in their development and industrial applicability. Therefore, the work has focussed on adaptations of ordinary ceramic processing as used by most ceramic component producers. The adaptations being developed involve mainly pretreatments of the starting materials and, in some cases post sintering treatments.

The systems chosen for study consisted of $A\ell_2O_3$ matrix reinforced with particles based on Co and Ti. The preliminary studies reported here involve investigations with starting metal particles with approximately spherical morphology.

It is difficult to simply incorporate a metallic inclusion in a ceramic matrix prior to sintering: the problems that were encountered include:

1. Thermal expansion (TE) mismatch leading to microcracking
2. Oxidation of reinforcement
3. Melting or degradation of reinforcement at the sintering temperature
4. Detrimental reactions between inclusion and matrix producing unwanted phases
5. Degradation of interfaces during sintering.

These problems are being addressed by processing adaptations along four routes:

1. Development of special pretreatments for the ceramic powders as well as for the reinforcements
2. Optimisation of binding and sintering agents
3. Optimisation of compaction pressure

Within the constraints of the short time available, progress has been achieved and it has been shown that by the use of moderate pressure compaction, protective atmospheres and controlled sintering schedules, it is possible to include discrete metal particles in an $A\ell_2O_3$ matrix in such a way that they efficiently form crack bridges and enhance the energy dissipation characteristics of the ceramic.

Of the two metallic materials tried as reinforcement inclusions, Ti, although being a potentially good candidate material due to very small TE mismatch and good interface strength under ideal conditions, presented too many problems mainly due to its very high chemical reactivity at high temperatures. By the use of protective atmospheres during sintering it proved partly possible to avoid excess formation of extraneous intermetallic phases and oxides but it was soon decided to develop the more promising $A\ell_2O_3$/cobalt system.

The next sections present some details on the processing and microstructural development of the composites. At present, an $A\ell_2O_3$/10–20%Co composite appears to be the most promising but further processing development is essential.

2.1.1 Microstructural, compositional and interfacial development

The $A\ell_2O_3$ powder used was AKP 30 from SUMITOMO Chemical Co, Ltd, Japan. It has a very uniform morphology and a narrow grain size distribution as shown in Fig.3. One of the main advantages of this powder is its reactivity which has enabled full densification at relatively low temperatures. The properties provided by the manufacturers are shown in Table 1.

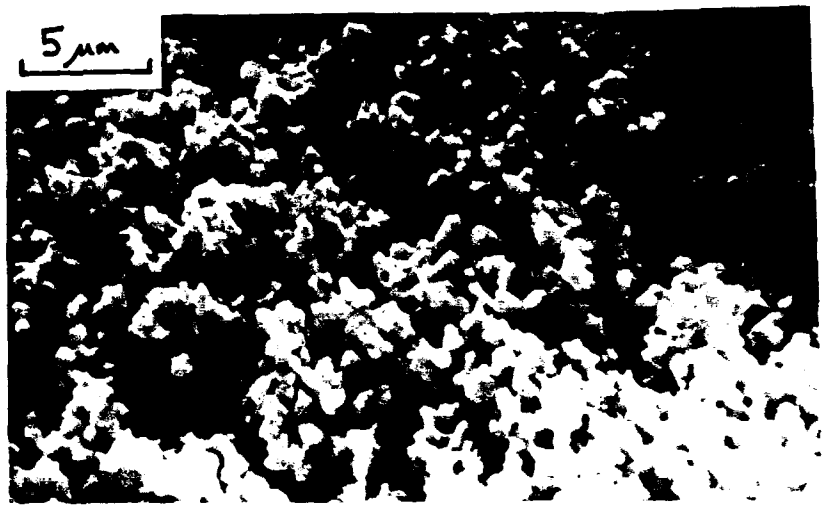

FIG.3 – Morphology of the Sumitomo AKP 30 pure $A\ell_2O_3$ powder.

Table 1: Some properties of the SUMITOMO AKP 30 $A\ell_2O_3$ used in this work

Powder form	Irregular
Crystal structure	Hexagonal (α)
Purity	>99.99%
B.E.T. Specific Area	5–10 m^2/g
Average particle size	0.3–0.5μm
Moisture loss at 150 °C	<0.2%
Moisture loss on ignition at 1000° C	<0.4%

After sintering, microstructural and compositional characterisation were carried out by optical and scanning electron microscopy (SEM) in conjunction with quantitative energy-dispersive X–ray (EDX) analysis and X–ray diffraction (XRD).

One of the basic prerequisites for a high strength ceramic is full densification. This is achieved usually by the use of small amounts of sintering aids and grain inhibitors. To achieve this without affecting the properties of the toughening particles a number of different combinations of binders and sintering aids were tried within a narrow range of processing conditions. Sintering behaviour and eventual densification depend critically on these conditions. As an example, the scanning electron micrographs shown in Fig.4 offer a comparison between: (a) poor densification after inadequate sintering; (b) relatively good sintering but poor densification; and (c) good sintering and densification. Optimum materials have grain size in the range between 0.5μm and 5μm which depends on the actual system.

The general morphology of one of the more promising $A\ell_2O_3$/Co composites (10% Co) is shown in the micrograph of the polished surface shown in Fig.5. The light areas are the metallic inclusions whereas the $A\ell_2O_3$ matrix appears darker. This material displays very low porosity, irregular inclusion shape, good distribution, and moderate interfacial integrity (the large variation in apparent inclusion size visible is due to variation in cross–section position).

As mentioned, one of the challenges in this work was balancing ideal sintering behaviour of the matrix with non–degradation of the metallic phase and good interfacial control. The fracture surface shown in the SEM micrograph of Fig.6 shows an example of the various problems encountered in an $A\ell_2O_3$/Ti composite even after controlled sintering. Various detrimental phases formed by the reaction of the metallic inclusions with the matrix are visible. The large globular phases have the spinel atomic structure, probably of the form MAl_2O_4 and the smaller globular structures are more complex metallic oxides. In many cases, notably in composites containing Ti or Ti alloys, it was very often found that it was very difficult to control the formation of complex

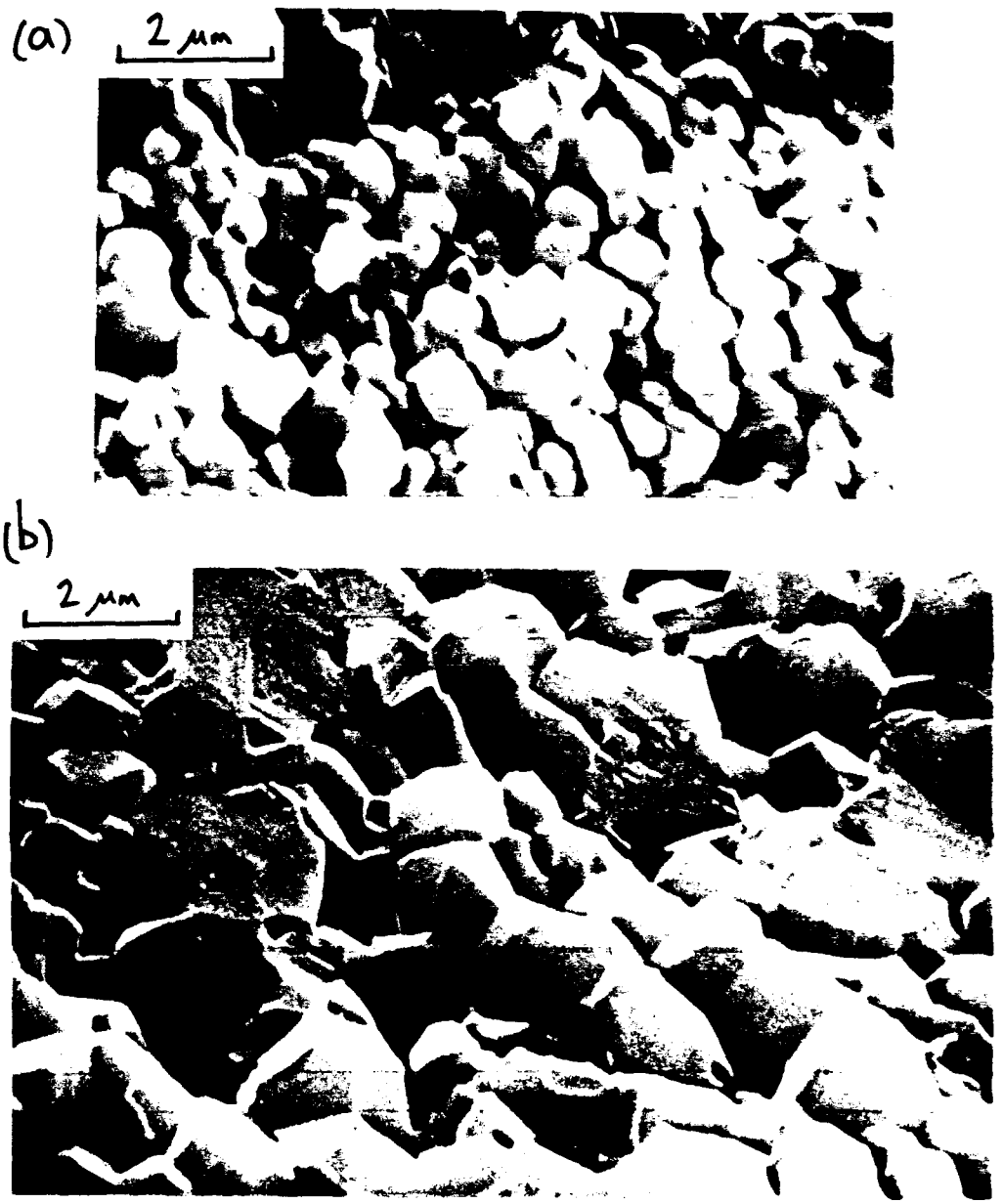

FIG.4 – Some examples of sintering behaviour of the Al_2O_3 matrix.
(a) poor sintering, due to inadequate sintering conditions (temperature, time etc) as well as interaction with the metallic inclusions;
(b) better sintering but poor densification leading to a wide grain size distribution, due to non–optimisation of sintering aids;

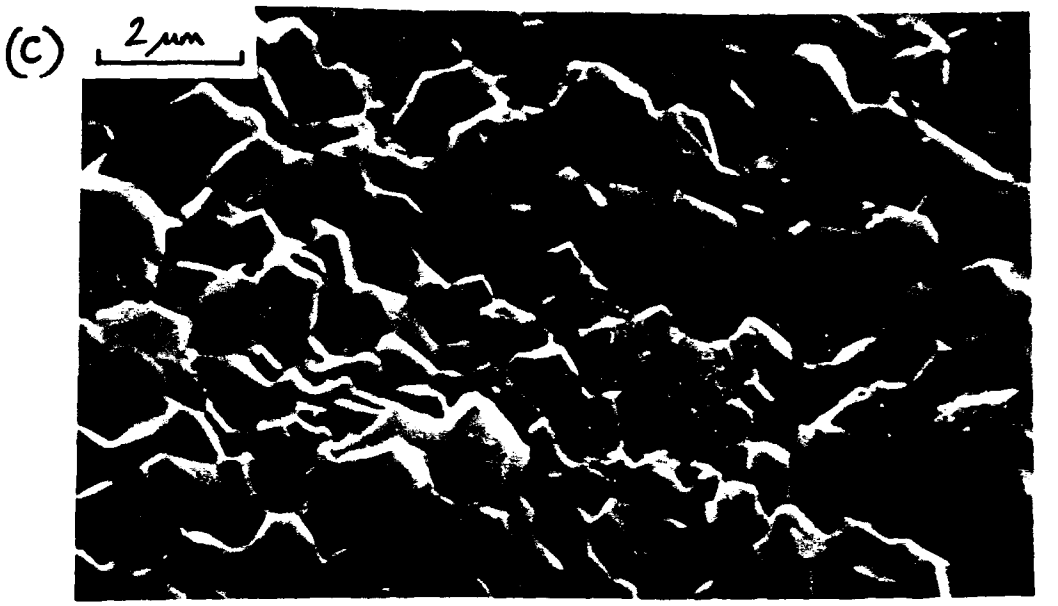

FIG. 4 (Continued)
(c) good sintering, densification and grain size distribution.

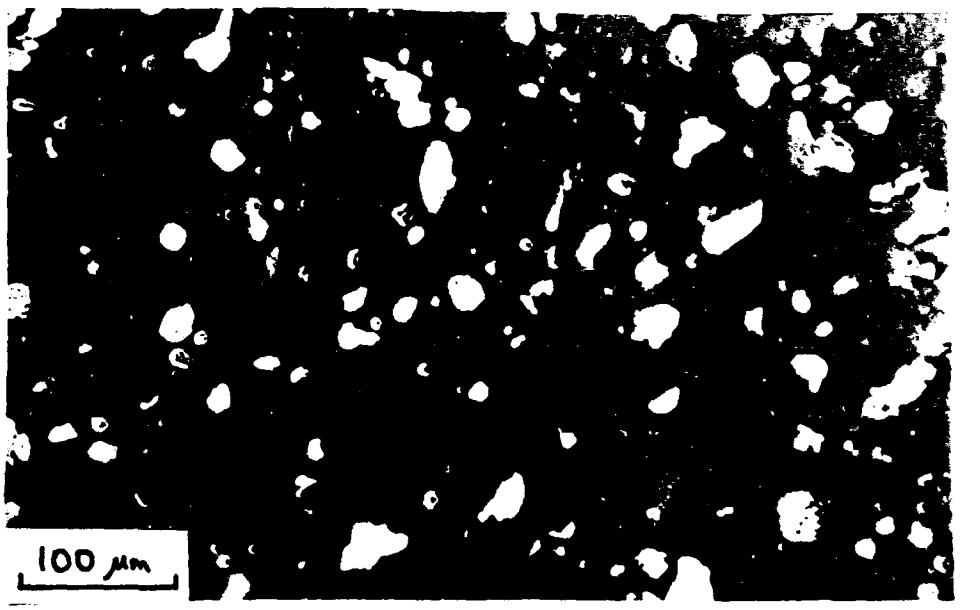

FIG.5 – Morphology of one of the $A\ell_2O_3$/10%Co composites developed in this work. Volume fraction of inclusions is 10%.

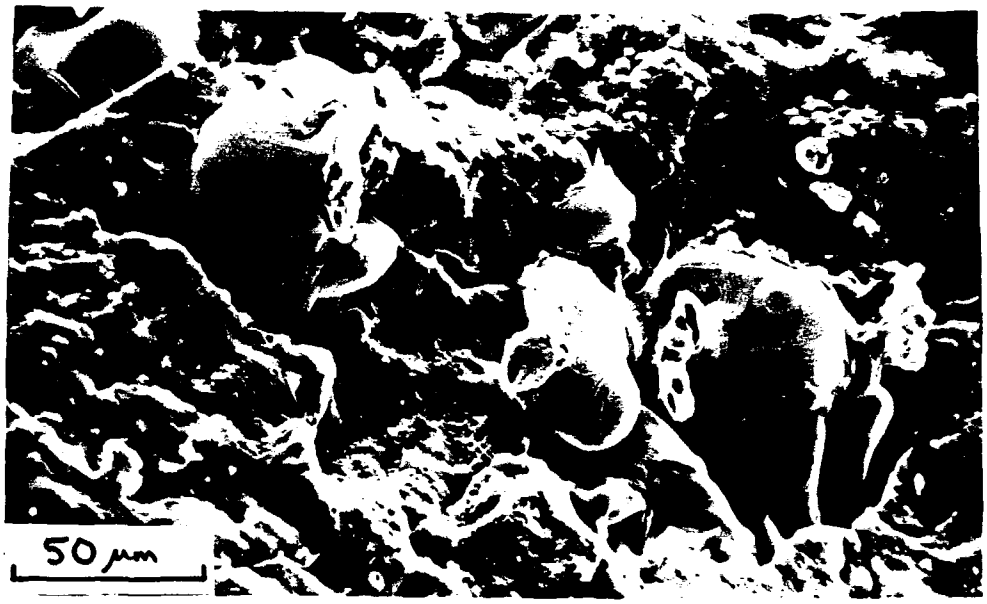

FIG.6 – Example of the formation of complex oxide structures due to the interaction of the inclusion with the matrix. Globular phase is probably $TiAl_2O_4$ (spinel).

intermetallics, especially aluminides such as $TiAl_3$ or Ti_3Al. The actual structures were often identified to consist of a core of Ti–rich metal surrounded by non–stoichiometric Ti_3Al followed by a layer of $TiAl_3$ close to the $A\ell_2O_3$ matrix. In many cases it was also found that the intermetallic phases formed were themselves surrounded by a layer of complex oxide, probably produced by direct interaction with the $A\ell_2O_3$ at the high sintering temperatures. Most of these extraneous phases are very hard and brittle and have a detrimental effect on the mechanical properties of the composite.

In many cases the formation of intermetallic phases, especially complex oxides, was accompanied by volumetric expansion which resulted in severe microcracking of the $A\ell_2O_3$ matrix as shown in Fig.7. In some specific cases formation of intermetallic phases was found to result in reduced volume, a fact which could potentially be utilised for introducing residual compressive stresses in the matrix of the final composite.

Grain size distribution in the specimens was determined by measurement of the average size of at least 100 grains by the linear intercept method. A representative example of the results obtained for one of the better–developed $A\ell_2O_3$/Co materials is shown in the histogram shown in Fig.8. It is obvious that, even though abnormal grain growth has not been eliminated completely, the grain size distribution is relatively narrow.

As shown in Fig.4c the predominant failure mode for well–sintered matrix is intergranular. This is in general agreement with published work for well–densified fine–grained $A\ell_2O_3$. In fact, transgranular fracture was only observed in cases of abnormal grain growth of over–sintered specimens as can be seen in Fig.4b. In certain applications however, mixed intergranular–transgranular fracture mode may offer specific advantages as has been shown in recent R–curve behaviour studies (e.g. Vekinis *et al.*, 1990).

Parallel work has also been carried out on control of the interface. The composites developed display low to moderate interfacial strength. The results, although preliminary, in general show that the processing technique offers potential for

FIG.7 – Microcracking due to swelling induced by the formation of an intermetallic phase surrounding a metal–rich inclusion.

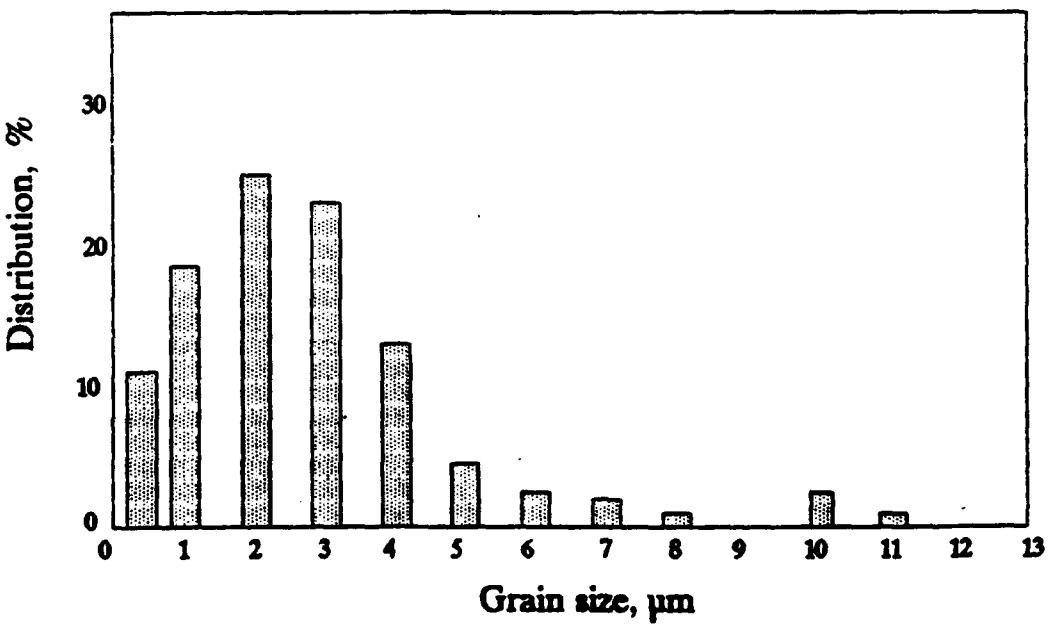

FIG.8 – Histogram of the $A\ell_2O_3$ grain size distribution of $A\ell_2O_3$/10%Co.

development of controlled interfaces.

Some of the microstructural properties of the $A\ell_2O_3$/10%Co material are tabulated in Table 2.

Table 2 – Some microstructural properties of the composites:

Properties of the $A\ell_2O_3$ matrix	
Purity	>99%
Open porosity	0–0.1%
Total porosity	<1%
Average grain size	1–5μm
Range of grain size (95%)	1–10μm
Fracture mode, % intergranular	>90%
Properties of the ductile inclusions	
Shape	Irregular
Bonding integrity	Moderate
Nature	Alloy or pure metal

2.2 Mechanical properties

Some combinations of processing conditions were found to give a promising composite which could be fabricated reproducibly. These were subjected to preliminary testing of their mechanical and fracture behaviour. This has concentrated on measurements of their modulus of rupture and SEM observations of fracture surfaces.

2.2.1 Modulus of rupture (MOR)

The modulus of rupture, MOR, (frequently now referred to as "transverse rupture strength") of the materials was measured in 3–point bending on individually produced short bar specimens. The dimensions were approximately 4x4x17 mm and the specimens were ground and polished to a parallelism of ± 5μm. The testing was carried out in an Instron universal testing instrument at a loading rate of 10μm/min.

The MOR was calculated from the well–known equations:

$$MOR_3 = \frac{Psd}{8I} \qquad (4)$$

where P is the fracture load (N), s the roller span, I the 2nd moment of area of the specimen = $bd^3/12$ for bar specimens, b the width of the specimen and d the height of the specimen.

The MOR of $A\ell_2O_3$/10%Co was measured to be approximately 185±6 MPa, compared with that of pure 99.5% $A\ell_2O_3$ specimens sintered to full density under identical conditions, which was measured to be 310±20 MPa. The MOR of $A\ell_2O_3$/20%Co specimens was found to be lower at 96±9 MPa. The lower MOR values for the reinforced specimens are to be expected as the metallic reinforcements do not at present have very strong interfaces with the $A\ell_2O_3$ matrix and so act as strength–reducing flaws. However, examination of the fracture surfaces shows that they offer promise for considerable energy dissipation during fracture.

2.2.2 Fracture surface observations

A number of fracture surfaces were examined in the SEM, if possible matching locations on opposite sides of the crack. Figure 9 shows some good examples of metallic particles displaying bridging behaviour in $A\ell_2O_3$/10%Co. The number of reinforcing particles displaying some type of bridging behaviour was, in the best cases developed, up to 50%. Figure 9a shows a necked Co particle which failed by final void formation. Figures 9b,c are stereo pairs (parallel–ray viewing) of opposite halves of a cobalt particle which failed by moderate decohesion and necking to a knife–edge. Such examples of "ideal" failure behaviour represent only about 20% of the Co particles however. In many other cases bridging was manifested by shearing of the particle with very little debonding or, in the other extreme, by frictional sliding due to very weak interfaces giving complete debonding. Optimisation of the metal–$A\ell_2O_3$ interface is required to give a higher percentage of "ideal" failures and thus maximum energy dissipation.

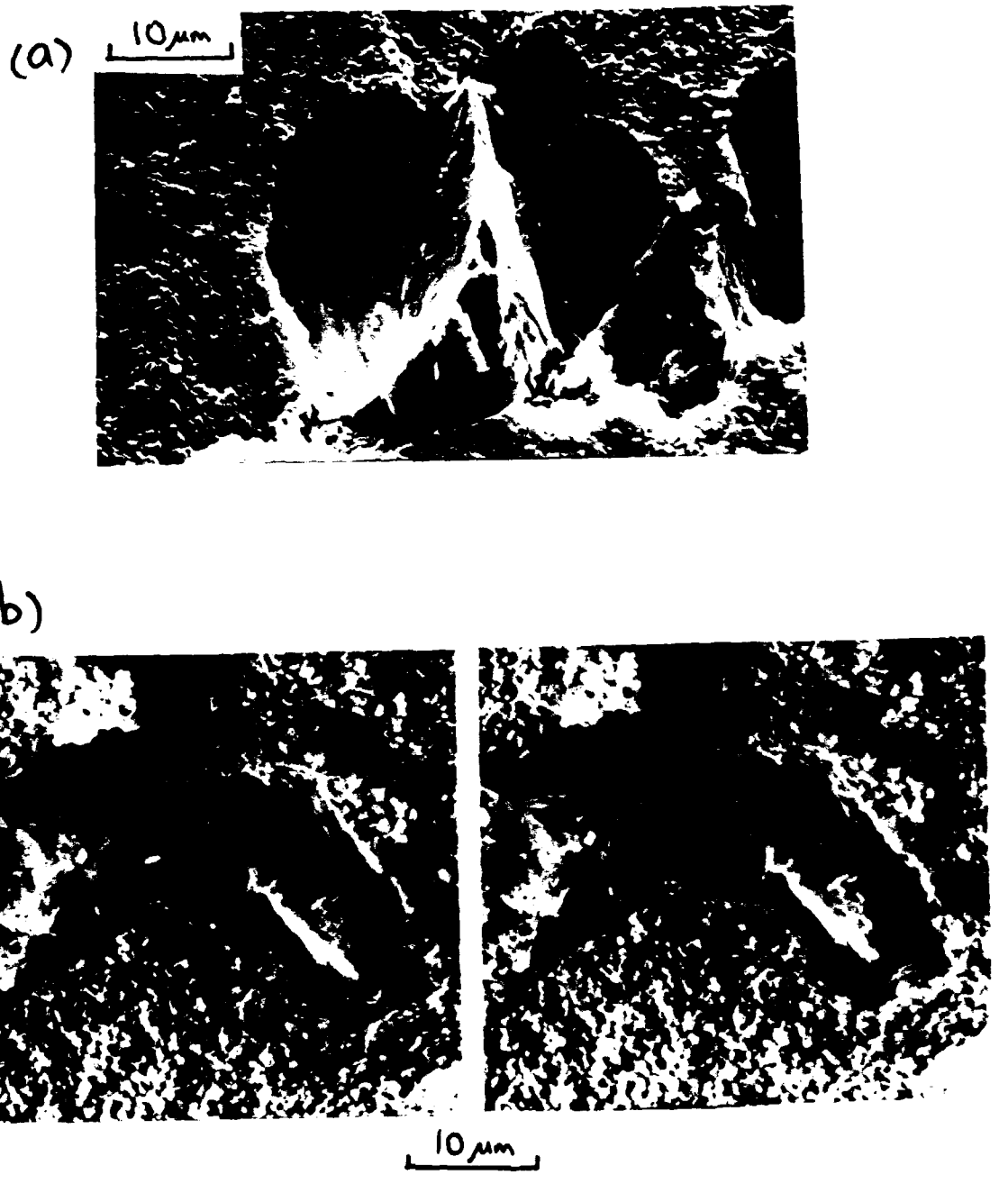

FIG.9 – Examples of crack bridging by intact cobalt particles in $A\ell_2O_3$/10%Co composite. (b) and (c) are stereo pairs (parallel–ray viewing) of opposite halves of a necked particle.

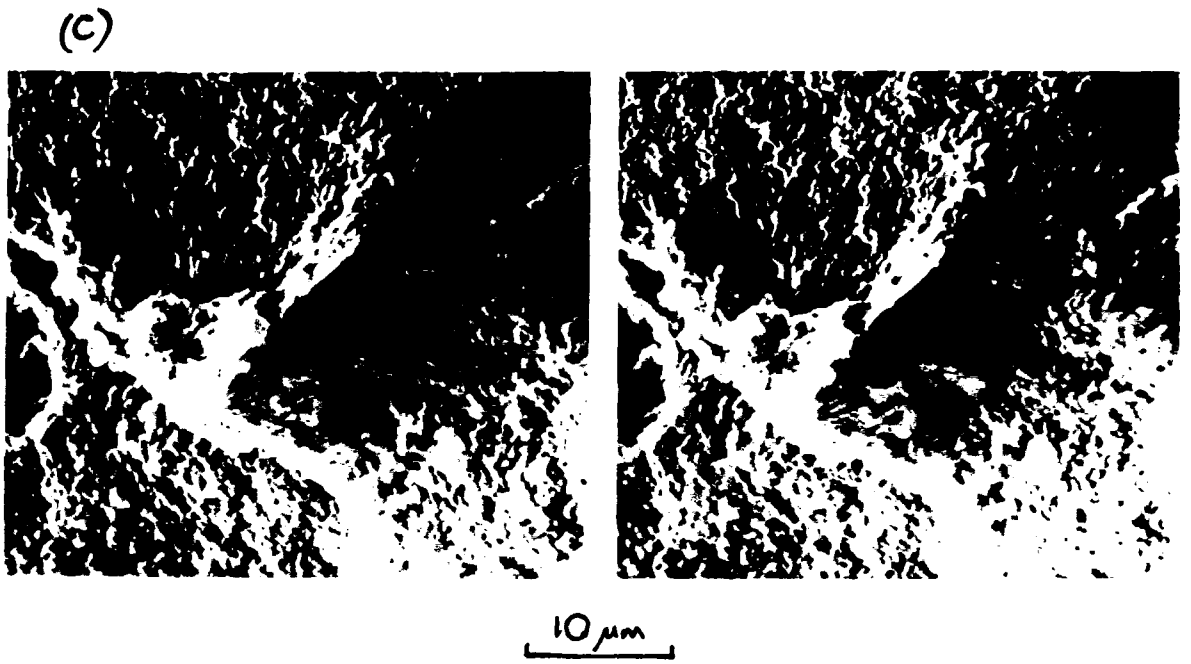

FIG.9 (Continued)

3. CONCLUSIONS

In conclusion, the preliminary studies carried out in this project show that there is strong potential for development of metal particle–reinforced $A\ell_2O_3$. The most important aspects of the work that need to be addressed further are:

(1) Interfacial strength and integrity of interface.

(2) Chemical interaction of matrix with reinforcement.

(3) Toughening behaviour of the composite: fracture micromechanisms and R–curve behaviour.

REFERENCES

Aghajanian M.K., MacMillan N.H., Kennedy C.R., Luszcz S.J. and Roy R. (1989), J.Mats.Sci.24, pp.658–670.

Ashby M.F., Blunt F.J. and Bannister M.K. (1989), Acta metall.37, pp.1847–1857.

Bannister M.K. and Ashby M.F. (1991), Acta metall.mater.39, pp.2575–2582.

Bannister M.K., Shercliff H.R., Bao G., Zok F. and Ashby M.F. (1992), Acta metall. mater.40, pp.1531–1537.

Besson J., De Graef M., Lofvander J. and Spearing S.M. (1992), J.Mats.Sci., in press.

Cao H.C., Dalgleish B.J., Deve H.E., Elliott C., Evans A.G., Mehrabian R. and Odette G.R. (1989), Acta metall. 37(11), pp.2969–2977.

Cox B.N. (1991), Acta metall. mater. 39(6), pp.1189–1201.

Cox B.N. and Lo C.S. (1992a), Acta metall. mater. 40(1), pp.69–80.

Cox B.N. and Lo C.S. (1992b), Acta metall. mater., in press.

Cox B.N. and Marshall D.B. (1991), Acta metall. mater. 39(4), pp.579–589.

Deve H.E., Evans A.G., Odette G.R., Mehrabian R., Emiliani M.L. and Hecht R.J. (1990), Acta metall. mater. 38(8), pp.1491–1502.

Deve H.E. and Maloney (1991), Acta metall. mater. 39(10), pp.2275–2284.

Evans A.G. and McMeeking R.M. (1986), Acta metall.34, pp.2435–2441.

Flinn B.D., Ruhle M. and Evans A.G. (1989), Acta metall. 37(11), pp.3001–3006.

Krstic V.V., Nicholson P.S. and Hoagland R.H. (1981), J.Am.Ceram.Soc.64, p.499.

Lu T.C., Evans A.G., Hecht R.J. and Mehrabian R. (1991), Acta metall. mater. 39(8), pp.1853–1862.

Lueth R.C. (1974), Fracture Mechanics of Ceramics, eds. Bradt R.C. *et al.*, vol 2, Plenum Press, New York, p.791.

Mykura N. (1992), in Advanced Materials Technology International, ed. David Whittaker, Sterling Publications, London.

Newkirk M.S., Lesher H.D., White D.R., Kennedy C.R., Urquhart A.W. and Claar T.D. (1987), Ceramic Engineering Science Proceedings 8(7–8), pp.879–885.

Newkirk M.S., Urquhart A.W. amd Zwicker H.R. (1986), J.Mats.Res.1(1), pp.81–89.

Shaw M.C., Marshall D.B. and Evans A.G. (1990), Mat.Res.Soc.Symp.Proc.Vol.170, pp.25–31.

Sigl L.S. and Exner H.E. (1987), Metall.Trans.18A, p.1299.

Sigl L.S., Mataga P.A., Dalgleish B.J., McMeeking R.M. and Evans A.G. (1988), Acta metall. 36(4), pp.945–953.

Sun X., Trusty P.A., Yeomans J. and Shercliff H.R. (1991), Proc. ICCM7, Hawaii, June 1991.

Venkatsewara Rao K.T., Odette G.R. and Ritchie R.O. (1992), Acta metall. mater. 40(2), pp.353–361.

Vekinis G., Ashby M.F. and Beaumont P.W.R. (1990), Acta metall.38, pp.1151–1162.